Supplementary Information (SI) for EES Batteries.

Supplementary information for

Nonuniform charging and phase front instability in nickel (oxy)hydroxide thin-film electrodes

Aleksandr Kurilovich,[a,#] Avihay Ben Shitrit,[a,#] David S. Ellis,[a,#] Nadav Port,[b] Nir Gavish,[c] Arik Yochelis,[b,d,*] and Avner Rothschild[a,e,f,*]

[a] Department of Materials Science and Engineering, Technion - Israel Institute of Technology, Haifa, Israel

[b] Department of Physics, Ben-Gurion University of the Negev, Be'er Sheva 8410501, Israel

[c] Department of Mathematics, Technion - Israel Institute of Technology, Haifa, Israel

[d] Swiss Institute for Dryland Environmental and Energy Research, Blaustein Institutes for Desert Research, Ben-Gurion University of the Negev, Sede Boqer Campus, Midreshet Ben-Gurion 8499000, Israel

[e] The Grand Technion Energy Program (GTEP), Technion - Israel Institute of Technology, Haifa, Israel

[f] The Stewart and Lynda Resnick Sustainability Center for Catalysis (RSCC), Technion – Israel Institute of Technology, Haifa, Israel

[#] These authors contributed equally: Aleksandr Kurilovich, Avihay Ben Shitrit, David S. Ellis

[*] Corresponding authors: Arik Yochelis (yochelis@bgu.ac.il) and Avner Rothschild (avnerrot@technion.ac.il)

S1. Electrochemical and operando optical imaging characterization of the additional Nickel hydroxide samples

This section contains the figures related to the electrochemical-operando optical imaging setup relying on “cappuccino” cell as well as the corresponding characterization results for ED1, ED2, SIL2, SIL4 samples, as referred to in the main text. The SIL2 sample was measured in the simpler “beaker” 3-electrode cell. More details can be found in the Methods section.

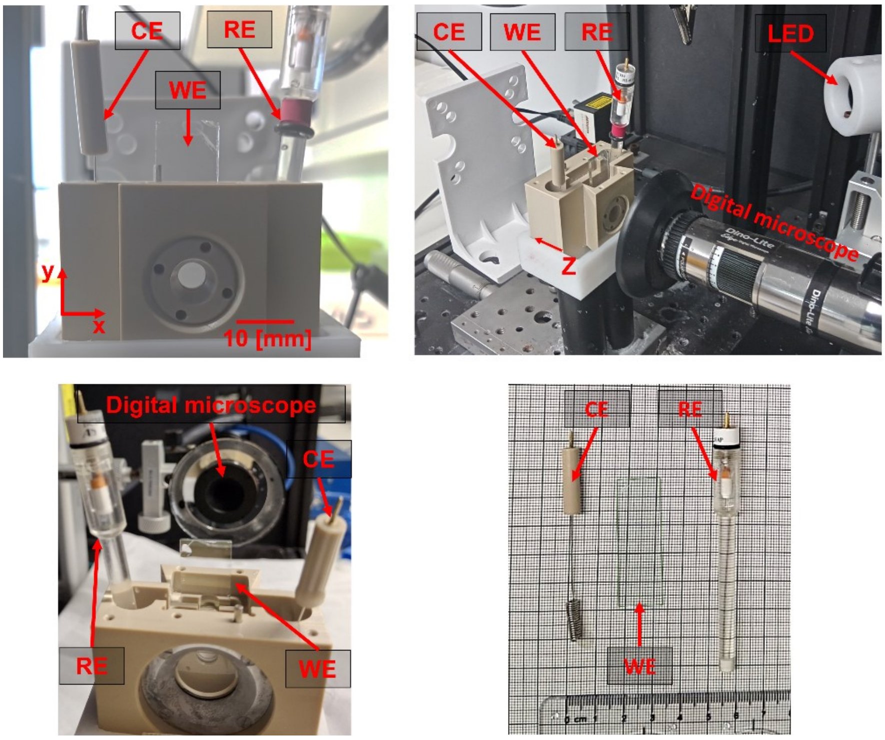

Figure S1. Experimental setup for operando optical imaging. Cappuccino cell with three electrodes in front of a digital microscope. WE: $Ni(OH)_2$ thin film electrode; RE: Hg/HgO reference electrode; CE: Pt wire counter electrode.

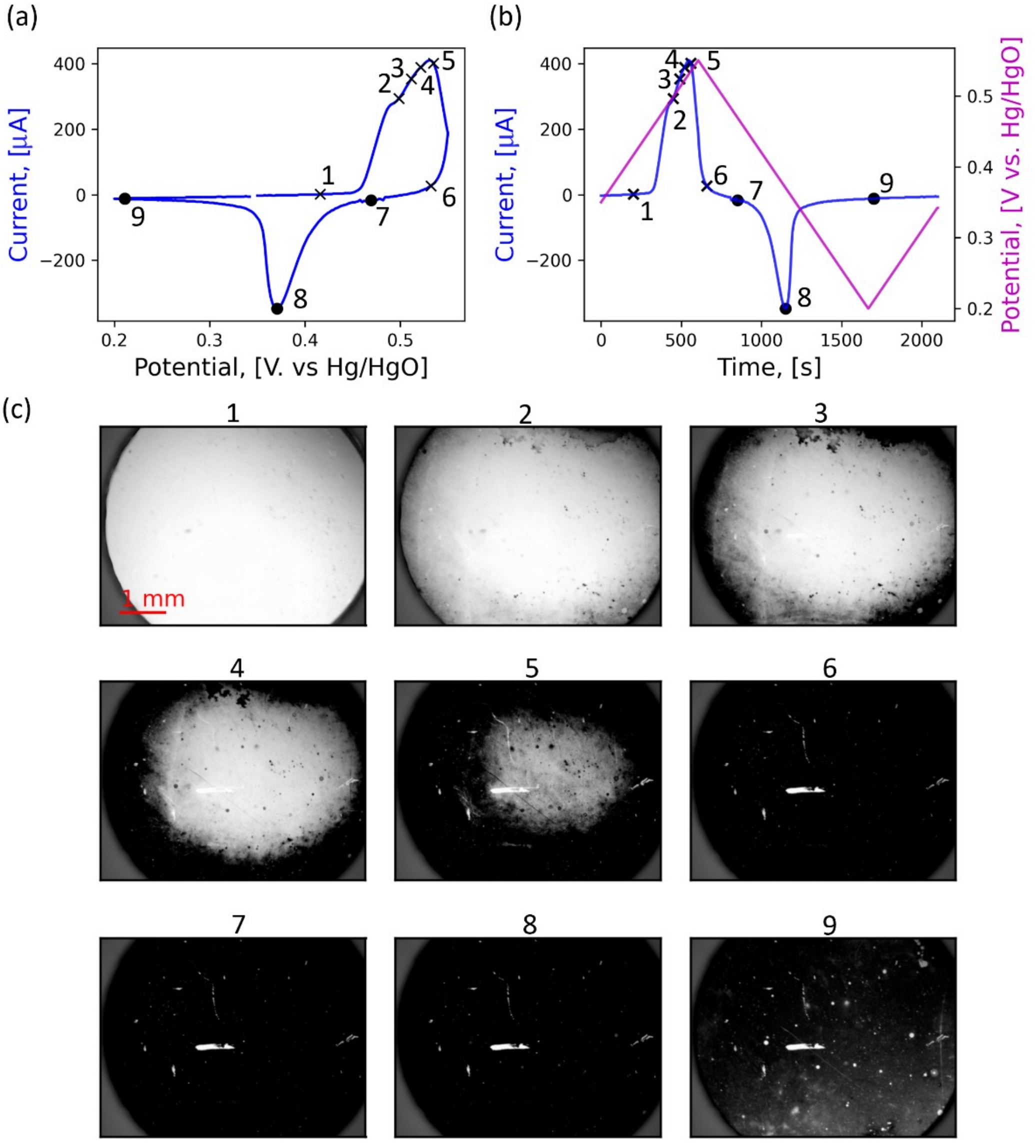

Figure S2. Lateral front propagation in electrodeposited electrode ED1. (a) CV scan between 0.2 and 0.6 V vs Hg/HgO, 0.33 mV s^{-1}, with selected points numbered 1-9. **(b)** The same data with current and potential presented as a function of time. **(c)** Gray scale video frames (from **Video 2**), measured in reflective mode, corresponding to the labelled points in panels (a) and (b).

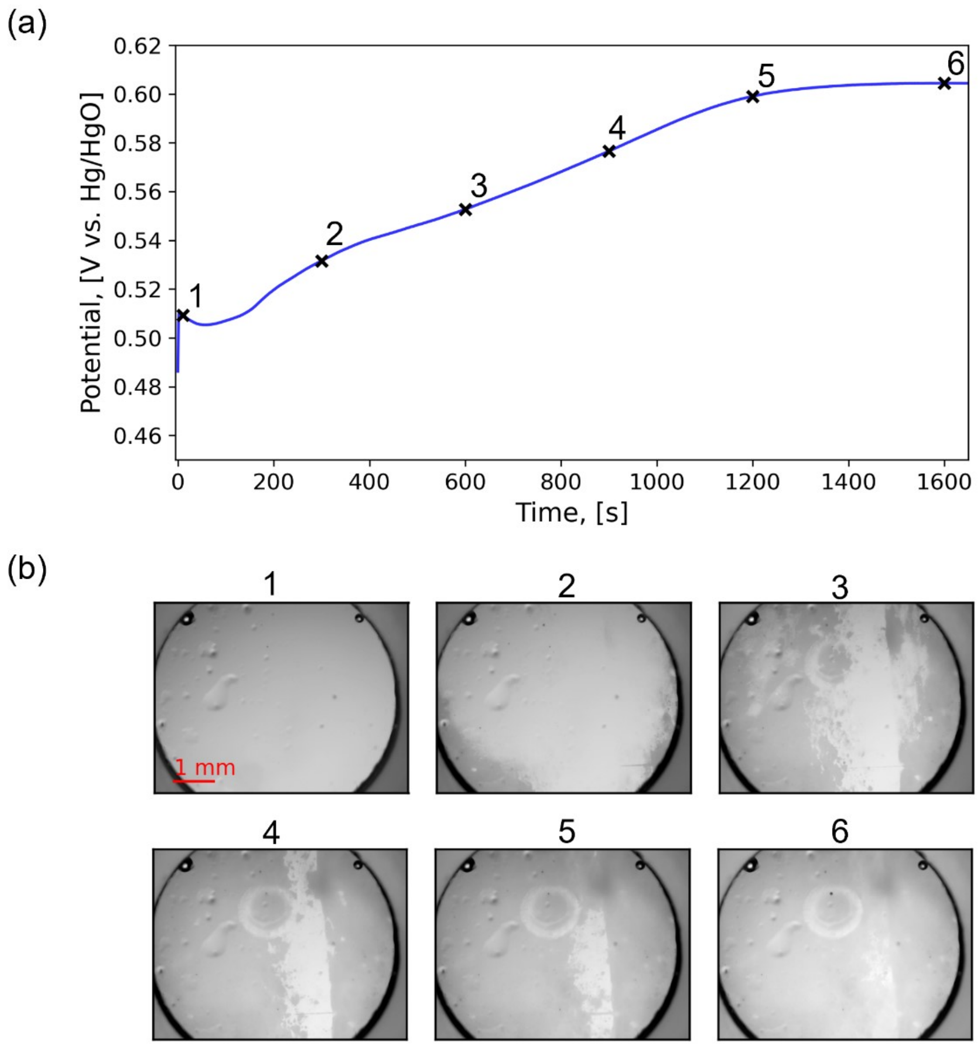

Figure S3. Lateral front propagation in electrodeposited electrode ED2. (a) Potential vs. time chronopotentiometry curve for galvanostatic charging at a constant current of 10 µA (35.7 µA cm^{-2}), with selected points numbered 1-6. **(b)** Gray scale video frames (from **Video 3**) corresponding to the labelled points in panel (a).

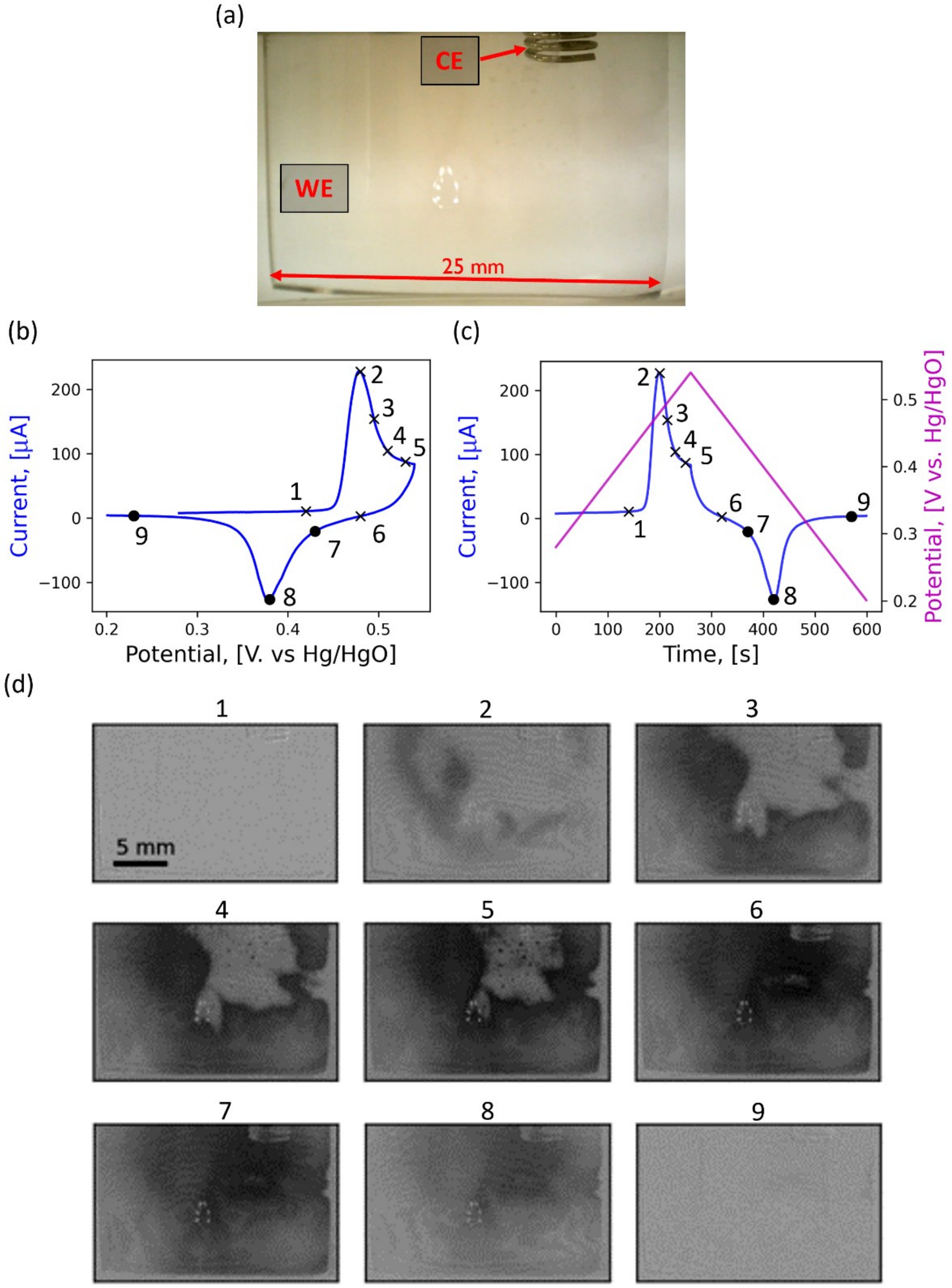

Figure S4. Lateral front propagation in a beaker cell. (a) A large area (25 mm wide) Ni(OH)$_2$ electrode SIL2 (labeled WE) in a beaker cell with Pt-wire counter electrode (CE, shown) and Hg/HgO reference electrode (not shown). **(b)** CV at potential sweep rate of 1 mV s^{-1}, with selected points numbered 1-9. **(c)** The same data with current and potential presented as a function of time. **(d)** Gray scale video frames (from **Video 4**) corresponding to the labelled points in panels (b) and (c), after subtraction of the first frame, with display enhanced for optimal contrast without causing saturation.

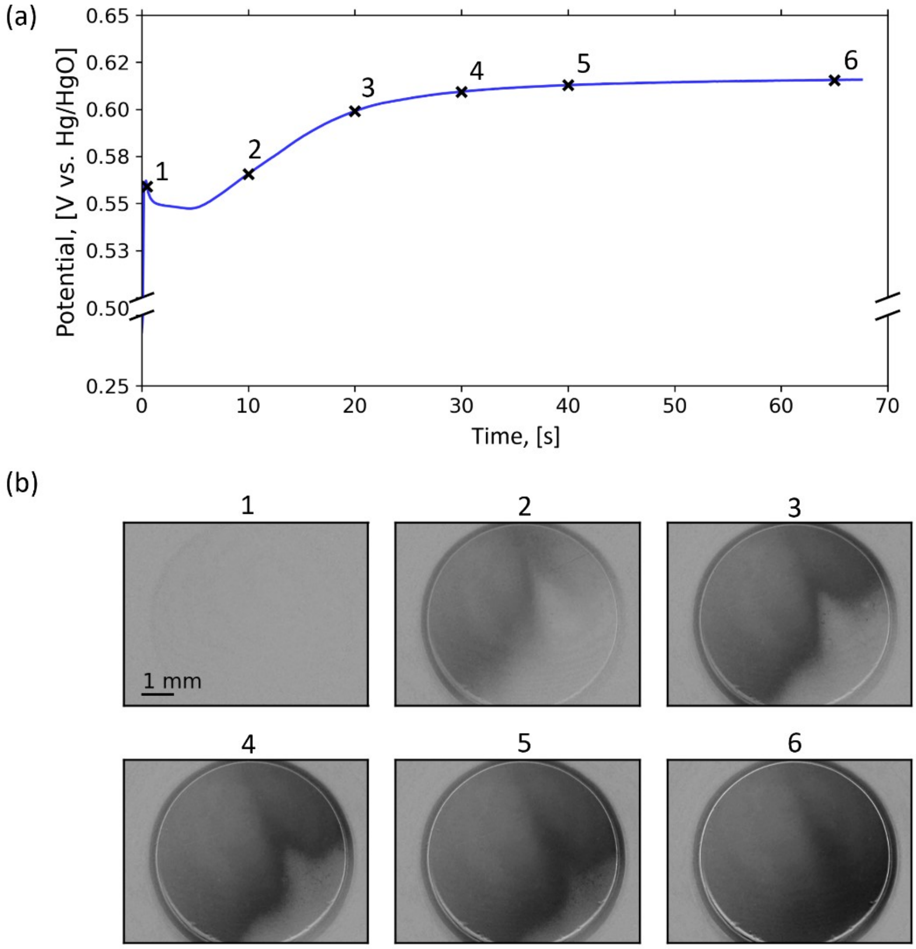

Figure S5. Diagonal front propagation in electrode SIL4. (a) Potential vs. time chronopotentiometry curve for galvanostatic charging of electrode SIL4 at a constant current of 100 µA (357.1 µA cm^{-2}), with selected points numbered 1-6. **(b)** Gray scale images (from **Video 6**) corresponding to the labelled points in panel (a), after subtraction of the first frame, with display enhanced for optimal contrast without causing saturation.

S2. Surface morphology and cross-section microstructure of SILAR-deposited $Ni(OH)_2$ electrodes

The surface morphology of SILAR-deposited $Ni(OH)_2$ electrodes was imaged by SEM and AFM to examine their uniformity. In addition, a cross-section TEM sample of an electrochemically cycled electrode which showed front propagation (**Figure S4** and **Video 4**) was prepared by FIB and imaged by TEM, HAADF and EDS mapping, and analyzed by EELS, to examine the $Ni(OH)_2$ layer thickness, uniformity, microstructure and chemical composition.

Scanning Electron Microscopy (SEM)

The surface morphology of a bare ITO-coated glass substrate is presented in **Figure S6(a)**, showing uniform granular morphology of the ITO layer. After 100 SILAR deposition cycles of $Ni(OH)_2$, the surface morphology remained uniform, indicating full coverage of the $NI(OH)_2$ layer, as shown in **Figure S6(b)**. 100 cycles were chosen instead of the usual 50 in order to extenuate any possible defects and non-uniformities stemming from the deposition.

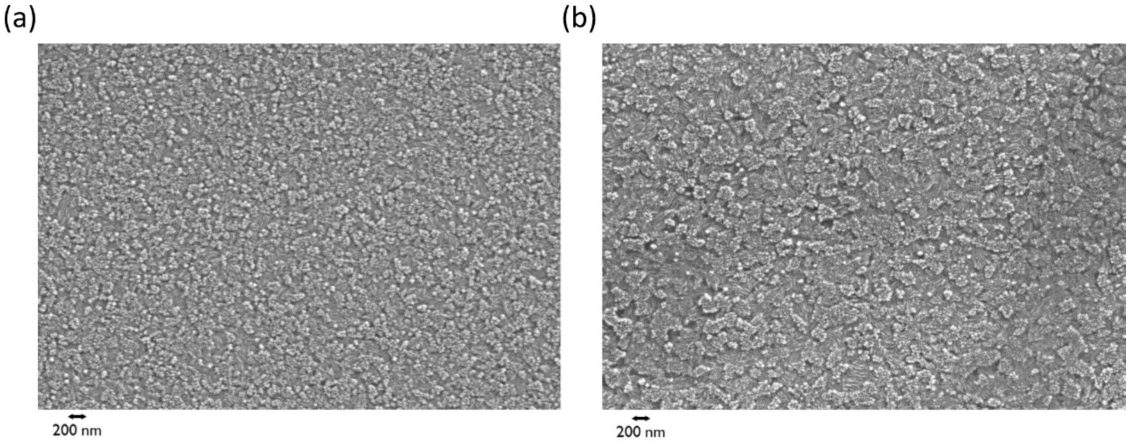

Figure S6: SEM micrographs of **(a)** bare ITO-coated glass substrate (before $Ni(OH)_2$ deposition), and **(b)** $Ni(OH)_2$ coated electrode after 100 SILAR deposition cycles. Both micrographs are representative of the imaged areas.

Atomic Force Microscopy (AFM)

AFM micrographs were measured in 3 random spots for the following samples: bare ITO-coated glass substrate after plasma treatment that preceded $Ni(OH)_2$ deposition, **Figure S7(a)**; $Ni(OH)_2$ electrode in the as-deposited state after 50 SILAR deposition cycles, **Figure S7(b)**; $Ni(OH)_2$ electrode (**SIL4**, deposited by 50 SILAR deposition cycles) after electrode formation by 200 CV cycles, **Figure S7(c)**. **Figure S7(d)** presents height distribution histograms of the respective AFM images (**Figures S7(a) – S7(c)**), and **Table S1** presents the surface roughness (R_q) values measured at 3 random spots across these samples, their average and standard deviation values. The surface roughness increases from 3.4±0.3 nm for the bare ITO substrate to 9.0±1.2 nm after SILAR deposition and 12.3±3.9 after electrode formation. This is also reflected in the height distribution histograms that become broader after SILAR deposition and electrode formation (**Figure S7(d)**).

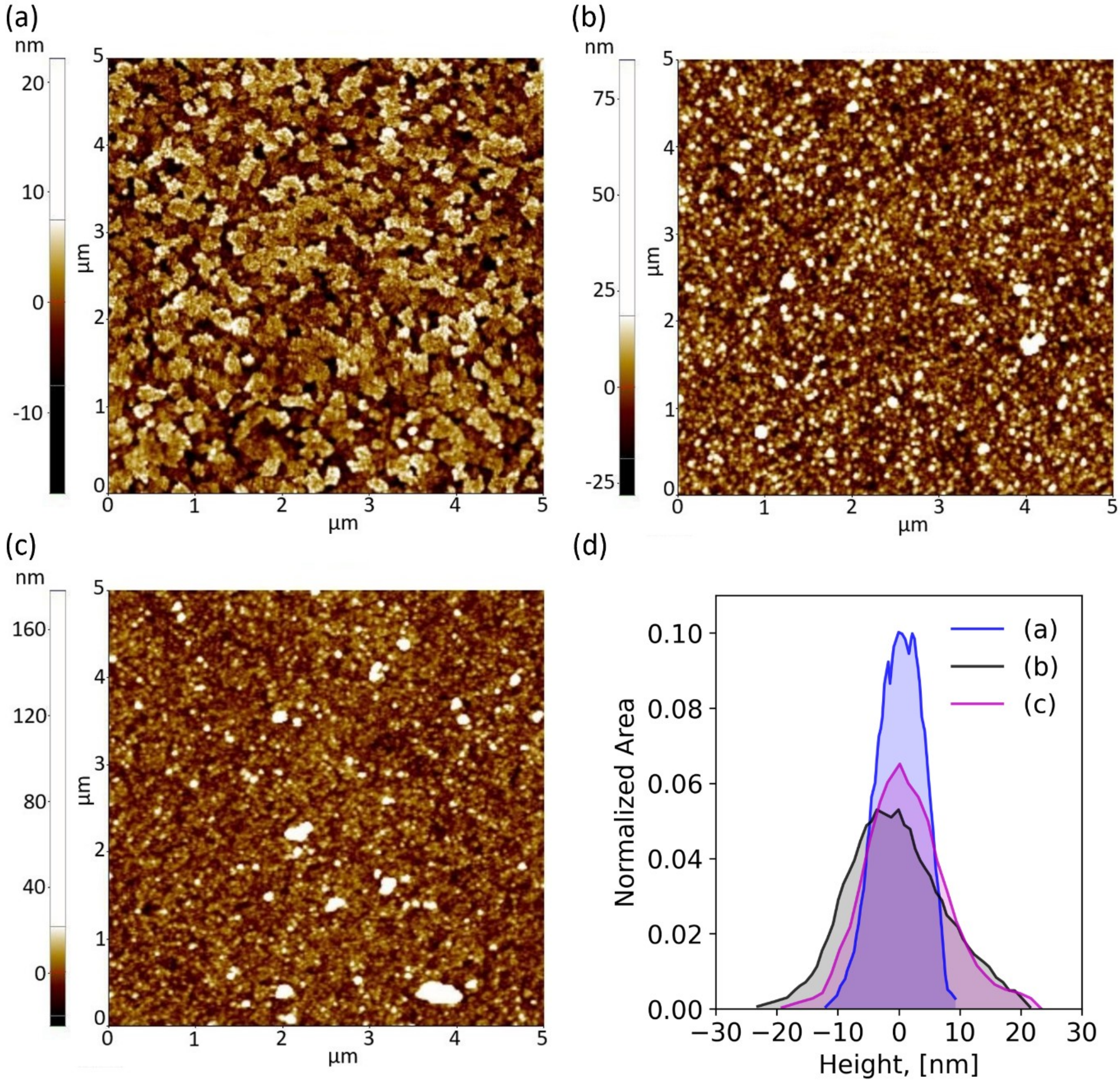

Figure S7: AFM micrographs of **(a)** Bare ITO substrate after plasma cleaning. Average surface roughness, R_q = 3.8 nm; **(b)** As-deposited $Ni(OH)_2$ electrode deposited by SILAR (50 deposition cycles). R_q = 9.5 nm; **(c)** SIL4 electrode (50 SILAR deposition cycles) after electrode formation by 200 CV cycles (0.2-0.54 V vs. Hg/HgO at 2 mV s^{-1}) in 1M KOH electrolyte. R_q = 10.7 nm. **(d)** Height distribution histograms (area-normalized) of the AFM images presented in panels (a)-(c).

Table S1: The surface roughness of a bare ITO substrate, as-deposited and electrochemically activated $Ni(OH)_2$ electrodes (Figure S7).

Electrode #/Measurment spot	**1 Rq [nm]**	**2 Rq [nm]**	**3 Rq [nm]**	**Average [nm]**	**STD [nm]**
Bare ITO surface (after plasma cleaning)	3.2	3.8	3.2	**3.4**	**0.3**
$Ni(OH)_2$ surface (as deposited)	7.6	9.5	9.8	**9**	**1.2**
$Ni(OH)_2$ surface after 200 CV cycles	9.6	10.7	16.8	**12.3**	**3.9**

Cross-section Focused Ion Beam (FIB) and Transmission Electron Microscopy (TEM)

A cross-section TEM sample of SIL2 electrode (50 SILAR deposition cycles) which showed lateral front propagation by CV cycling between 0.2 and 0.54 V vs Hg/HgO (at a potential sweep rate of 1 mV s^{-1}), as shown in **Figure S4** and **Video 4**, was prepared by FIB. The location of the FIB probe is shown in **Figure S16**.

Figure S8 presents a cross-section SEM micrograph taken in the FIB microscope during the final stage of the lamella preparation. The cross-section image shows the glass substrate at the bottom of the image, coated by a ~125 nm thick ITO layer, coated by a ~25 nm thick $Ni(OH)_2$ layer (the darkest contrast in the micrograph), coated by a porous tungsten layer to protect the lamella sample during FIB processing. The $Ni(OH)_2$ layer looks uniform, conformally coating the ITO-coated substrate.

Figure S9(a) presents EDS elemental maps of In, Ni and W (yellow, blue and cyan, respectively) of the FIB lamella sample. Tungsten was used as a protective layer during the cross-section preparation by FIB, and the indium signal comes from the ITO layer on the glass substrate. The nickel map is conformal to the indium map. **Figure S9(b)** presents a HAADF TEM micrograph of the same sample.

Figure S10(a) presents HRTEM micrograph of the $Ni(OH)_2$ layer, showing crystalline domains of few nm length scale. Three of these regions are magnified in **Figure S10(b)**, showing lattice periodicities consistent with d-spacings of the β-$Ni(OH)_2$ phase. However, we note that these lattice images were not aligned in their respective zone axis, therefore a reliable phase identification cannot be fully ascertained.

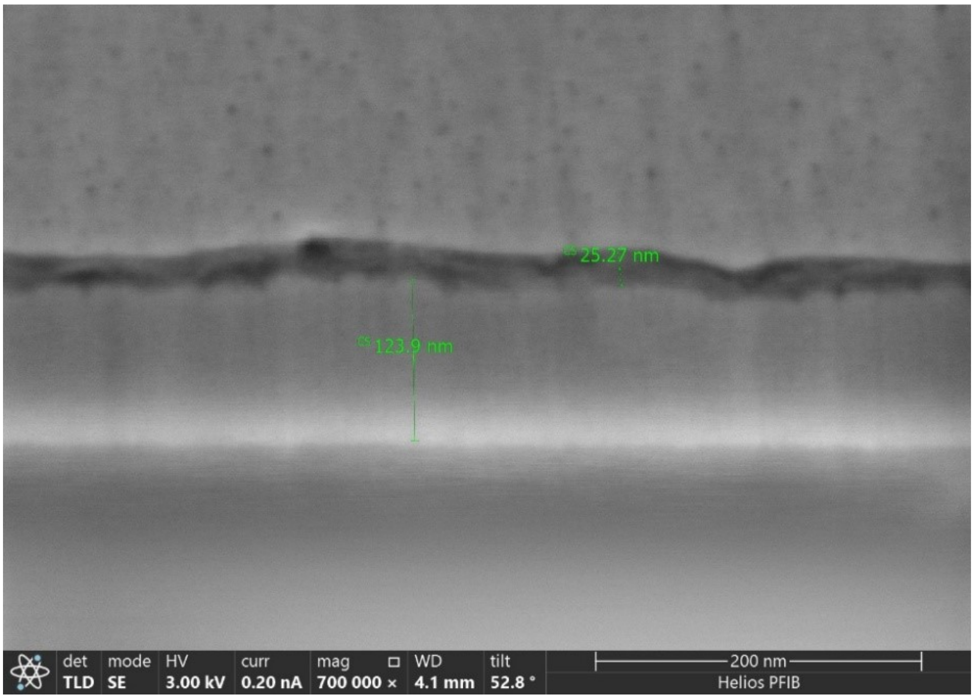

Figure S8: Cross-section FIB lamella extracted out of SIL2 electrode and imaged by secondary electrons during FIB sample preparation.

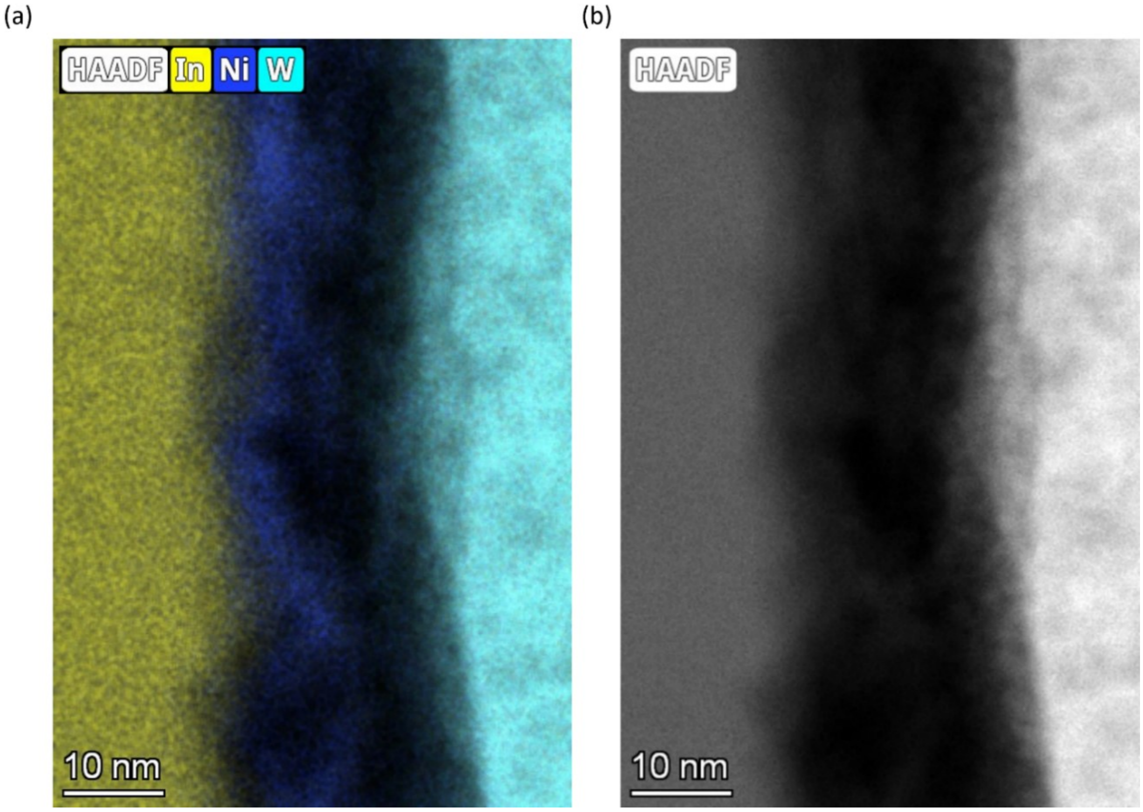

Figure S9: Cross-section EDS map (a) and **HAADF TEM micrograph (b)** of SIL2 electrode.

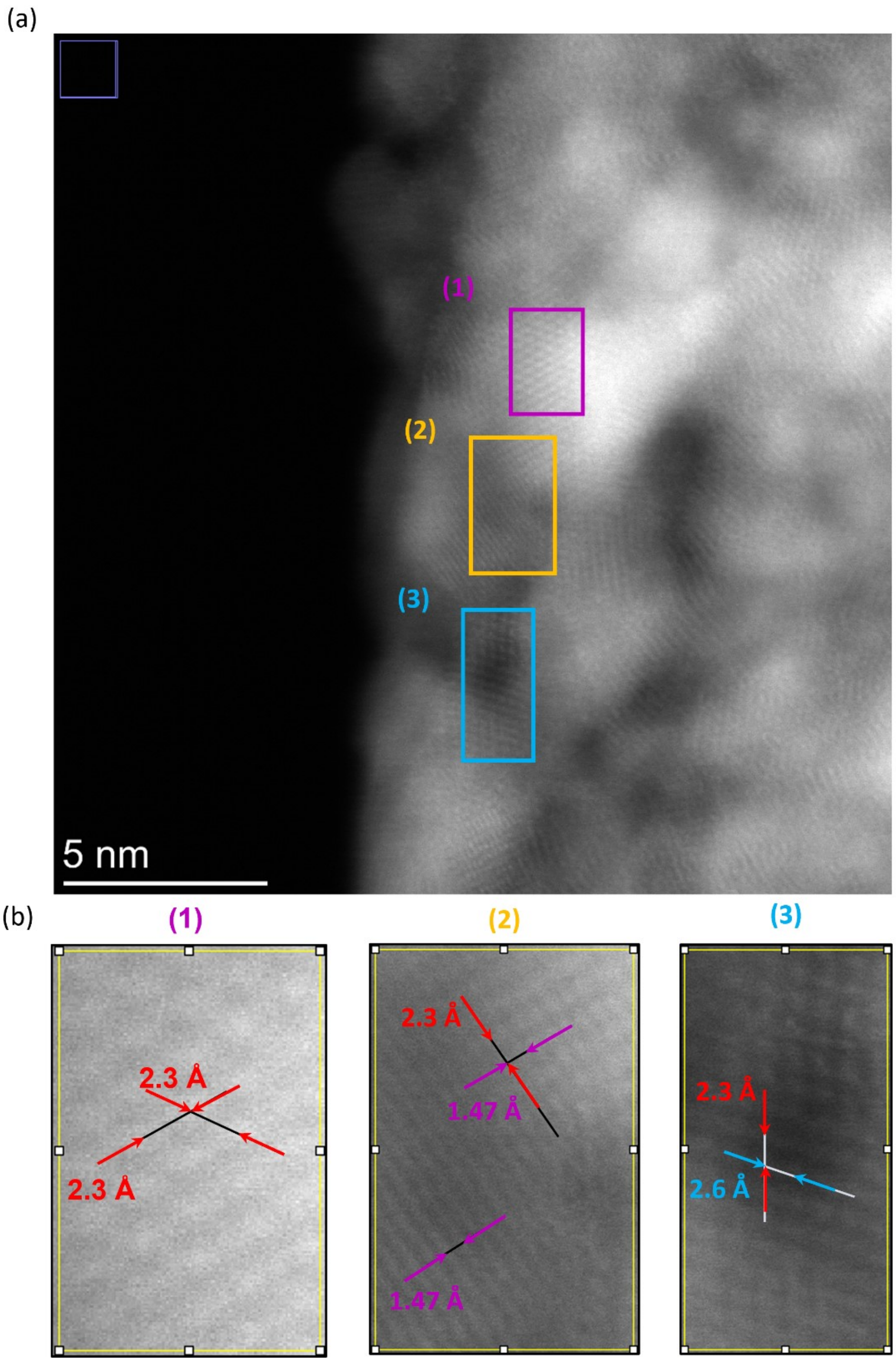

Figure S10: HRTEM lattice images of the Ni(OH)$_2$ layer in SIL2 electrode **(a)**, and magnified regions with crystalline domains **(b)**.

S3. Chemical and phase composition

The chemical and phase composition of $Ni(OH)_2$ electrodes were examined by EELS, RBS, and XRD.

Electron Energy Loss Spectroscopy (EELS)

The oxygen-edge EELS spectra of SIL2 electrode, after electrode formation by 200 CV cycles between 0.2 and 0.54 V vs Hg/HgO at 2 mV s^{-1}, corresponds to that of $Ni(OH)_2$ phase (with Ni in the oxidation state of Ni^{2+}), suggesting the layer is mostly in the uncharged Ni^{2+} state.

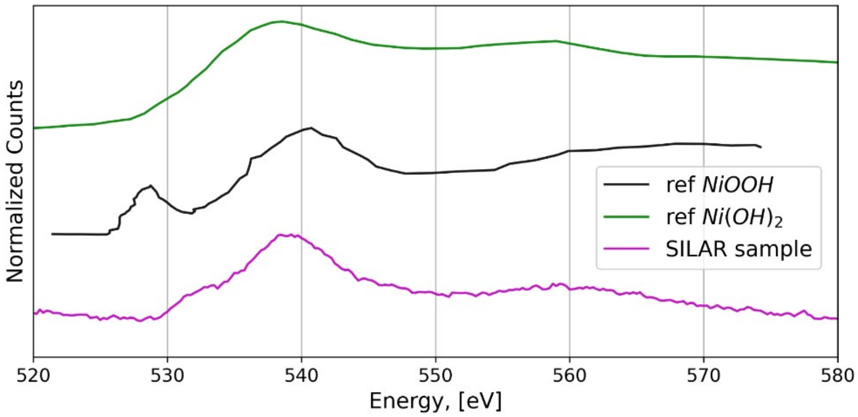

Figure S11: EELS spectra of SIL2 electrode (50 SILAR deposition cycles) after electrode formation by 200 CV cycles (purple curve), compared with references spectra of $Ni(OH)_2$ and NiOOH. The reference spectra are reported in ref. 1.

Rutherford Backscattering Spectrometry (RBS)

RBS spectra of SIL4 electrode (50 SILAR deposition cycles) before and after electrode formation by 200 CV cycles confirmed the $Ni(OH)_2$ stoichiometry. Interestingly, after CV cycling iron was detected, indicating that iron was incorporated into the $Ni(OH)_2$ electrode from iron impurities in the electrolyte.

RBS was also used to estimate the thickness of the $Ni(OH)_2$ layers in pristine $Ni(OH)_2$ electrodes deposited with different number of SILAR deposition cycles. 50 deposition cycles were correlated to ~52 nm thick $Ni(OH)_2$ layer.

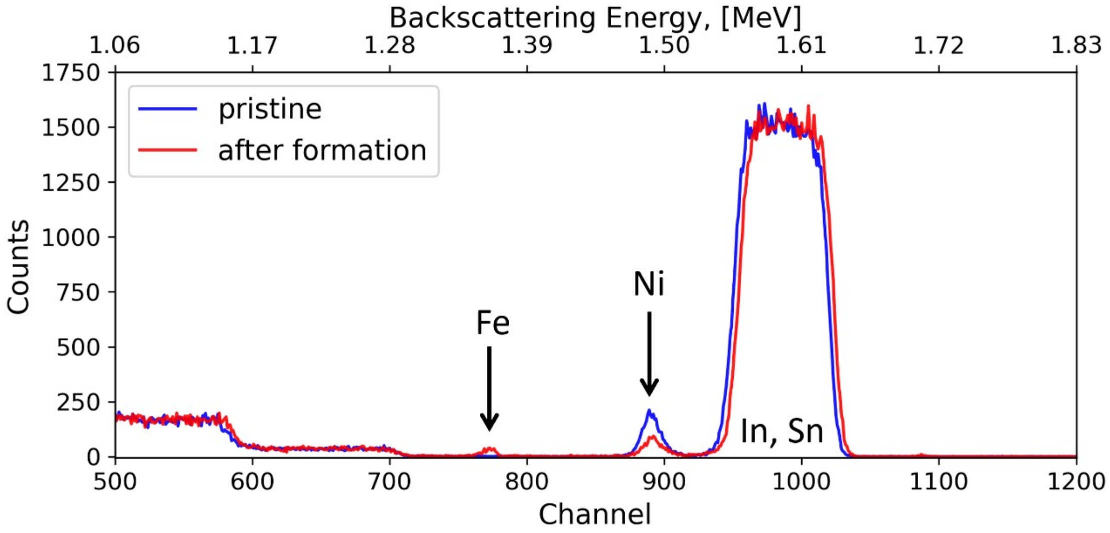

Figure S12: RBS spectra of SIL4 electrode before (as deposited) and after electrode formation by 200 CV cycles between 0.2 and 0.54 V vs Hg/HgO.

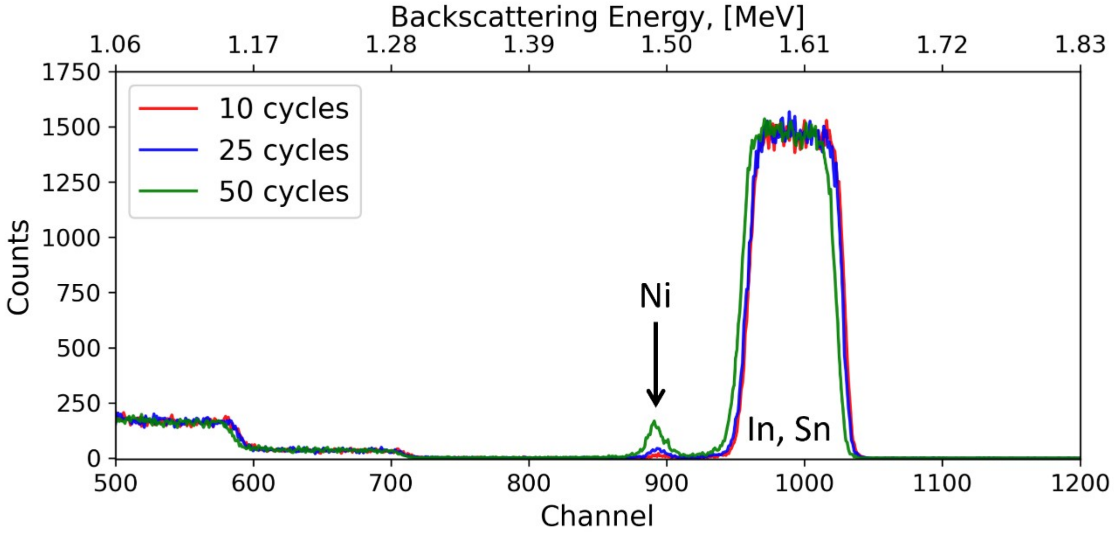

Figure S13: **RBS spectra** for SILAR deposited electrodes with 10, 25 and 50 deposition cycles**.**

Table S2. Summary of RBS analysis of as deposited Ni(OH)$_2$ electrodes.

Number of SILAR deposition cycles	**Areal density, 10^{15} at/cm^2**	**Thickness, nm**
#50	248.7±0.5	51.7±0.05
#25	93.2±0.5	20.0±0.05
#10	14.9±0.5	3.0±0.05

X-ray diffraction (XRD)

Grazing incidence XRD spectrum of electrochemically cycled SIL2 electrode (50 SILAR deposition cycles) that showed lateral front propagation (**S4** and **Video 4**) did not show evidence of β-$Ni(OH)_2$ in spite of the sample being discharged, **Figure S14** yellow curve. The peaks at 2θ of 12.85° and 25.84° could be assigned to γ-NiOOH (grey curve). It is possible that some γ-NiOOH was formed by overcharging the electrode without completely discharging it. The absence of a clear β-$Ni(OH)_2$ signature could be the result of the small size of the crystallites, as seen in **Figure S10**, which could make the corresponding Bragg reflections in the XRD pattern too small to detect.[2]

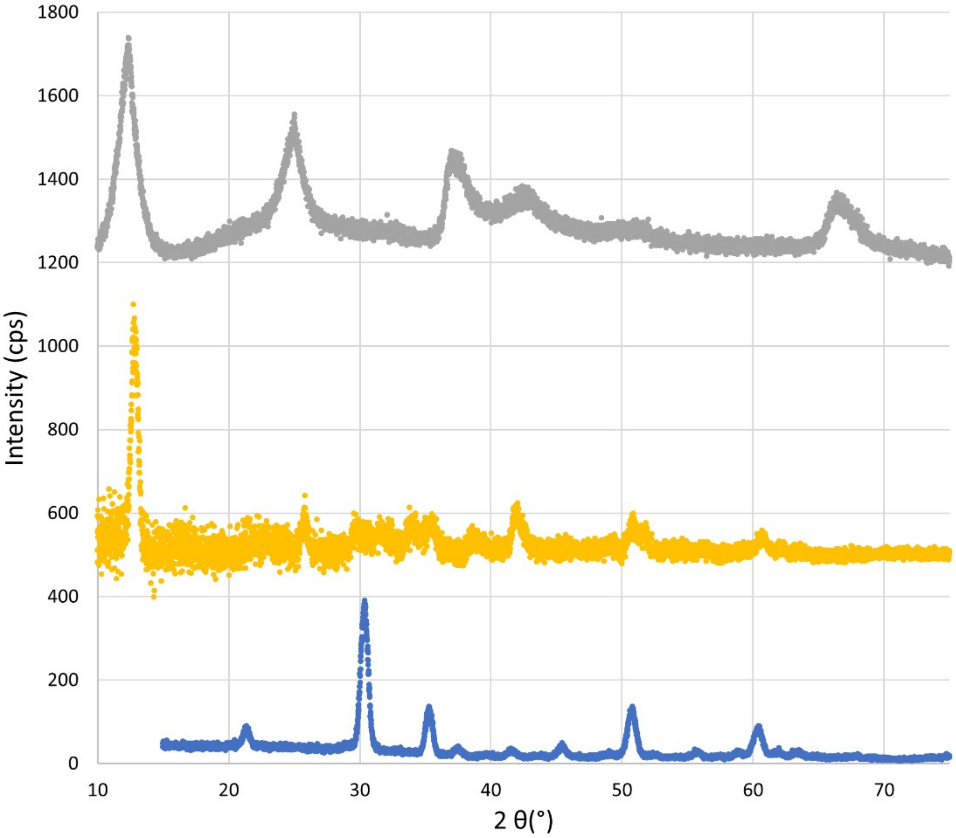

Figure S14: Grazing incidence XRD spectrum of $Ni(OH)_2$ electrode **SIL2** (50 SILAR deposition cycles) that showed lateral front propagation (yellow curve), bare ITO substrate (blue curve) and γ-NiOOH (grey curve).

S4. Thickness uniformity

The thickness uniformity of SILAR-deposited $Ni(OH)_2$ electrodes was examined by several techniques, including (i) X-ray reflectometry (XRR) of sample SIL1; (ii) spectroscopic reflectometry profiling at different points, millimeters apart of each other, looking for possible long-range thickness variations on SIL2 electrode; and (iii) RBS quantification (see **Section S3**, **Figure S13, Table S2**) of the thickness of different SILAR samples.

X-ray reflectometry (XRR)

While an X-ray reflectometry (XRR) measurement by itself does not provide an explicit value of uniformity, the measurement is taken at almost-grazing incident angle (Ω ~ 1°), thus covering a large area of the sample (>2 x 2 mm^2), and the observation of periodic interference fringes (**Figure S15**) indicates a consistent film thickness in the substantial area covered by the beam.

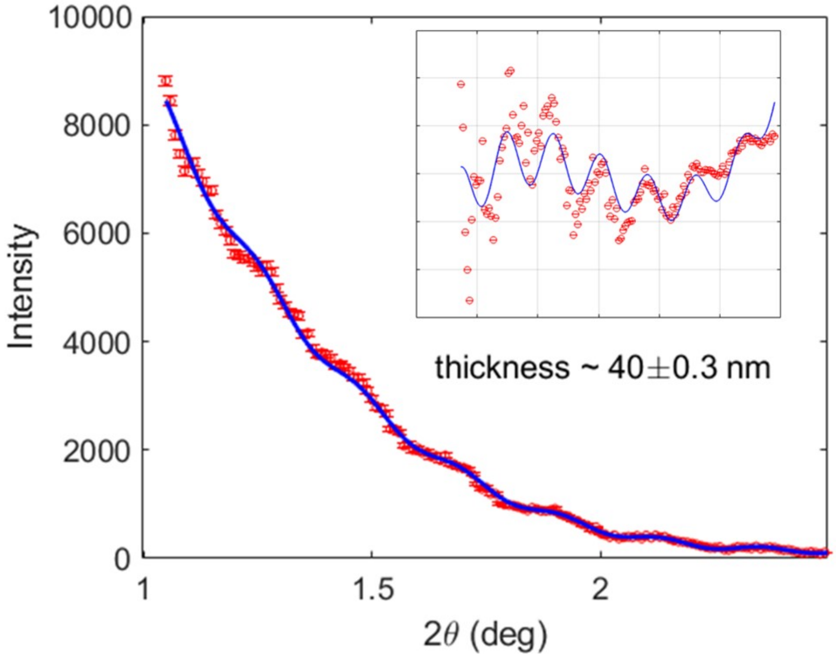

Figure S15: **X-ray reflectometry.** Ω-2θ scan of an as prepared $Ni(OH)_2$ electrode SIL1 deposited by SILAR (50 deposition cycles). The fit is to an exponentially decaying sinusoid superimposed with exponential and 3rd degree polynomial. To clarify the periodicity of the fringes, the data and fit with the exponential component subtracted are shown in the inset.

Spectroscopic reflectometry

The $Ni(OH)_2$ layer thickness was measured (postmortem) by spectroscopic reflectometry at the spots marked (a) through (j) in **Figure S16**, showing the $Ni(OH)_2$ electrode SIL2 (50 SILAR deposition cycles) inside the beaker in which its phase front propagation was recorded during CV cycles (**Figure S4**). The results are presented in **Table S3** in terms of the $Ni(OH)_2$ layer thickness measured at the (a) – (j) spots.

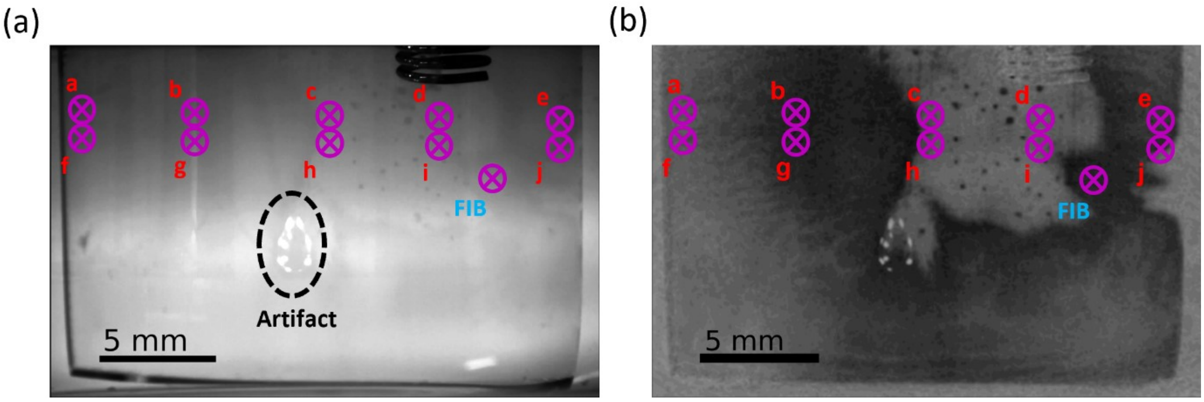

Figure S16: **Thickness uniformity. (a)** Grayscale video frame of electrode SIL2 during charging. **(b)** Difference frame with respect to the discharged state. Spots (a) - (j) mark the locations of spectroscopic reflectometry measurements across the electrode in the beaker CV measurements presented in **Figure S4**. FIB – location of the FIB probe (**Figure S8**). The artifact is attributed to the back reflection of the LED light source.

Table S3: $Ni(OH)_2$ layer thickness in spots (a) - (j) marked in Figure S16.

Spot	**Thickness**
a	43 nm
b	37 nm
c	39 nm
d	36 nm
e	50 nm
f	59 nm
g	41 nm
h	40 nm
i	48 nm
j	62 nm
Avg	**46 nm**
Stdv	**9 nm**

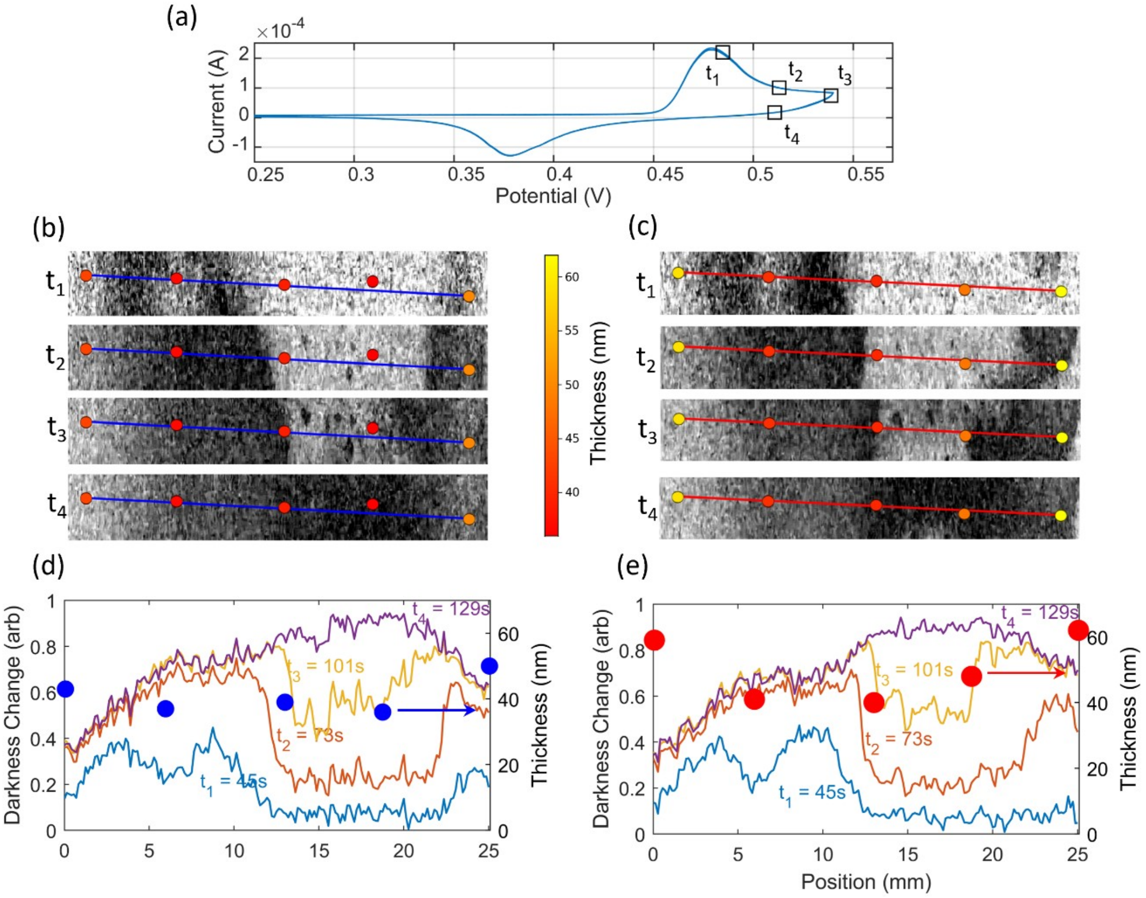

Figure S17. $Ni(OH)_2$ layer thickness and phase front propagation. (a) Cyclic voltammetry of electrode SIL2 measured in a beaker cell (**Figure S4**). **(b)** and **(c)**: Video frames (from **Video 4**) taken at different moments during the CV scan (labeled t_1 – t_4 in panel (a)) with overlaid $Ni(OH)_2$ layer thickness spots labeled (a) – (e) and (f) – (j), respectively, in **Figure S16**. **(d)** and **(e):** Darkness change profiles at different moments (t_1 – t_4) overlaid with the $Ni(OH)_2$ layer thickness spots (a) – (e) and (f) – (j), respectively.

S5. Iron impurity distribution

The iron impurity distribution in the $Ni(OH)_2$ layer was measured (postmortem) by dynamic Time-of-Flight Secondary Ion Mass Spectrometry (ToF-SIMS) at the spots marked (1) through (6) in **Figure S18(a)**, using the same $Ni(OH)_2$ electrode that was used for thickness uniformity mapping (electrode SIL2), after CV cycling (**Figure S4**). At each spot, the composition was analyzed using 25 keV Bi^+ primary ions in positive ion mode over 50 × 50 μm^2. Depth profiling was performed by sputtering using 1 keV O_2^+ ions over an area of 400×400 μm^2 (cation analysis). **Figure S18(b)** presents an optical image recorded after the ToF-SIMS analysis at one of the analyzed spots, showing the sputtered crater and the measured area within the crater.

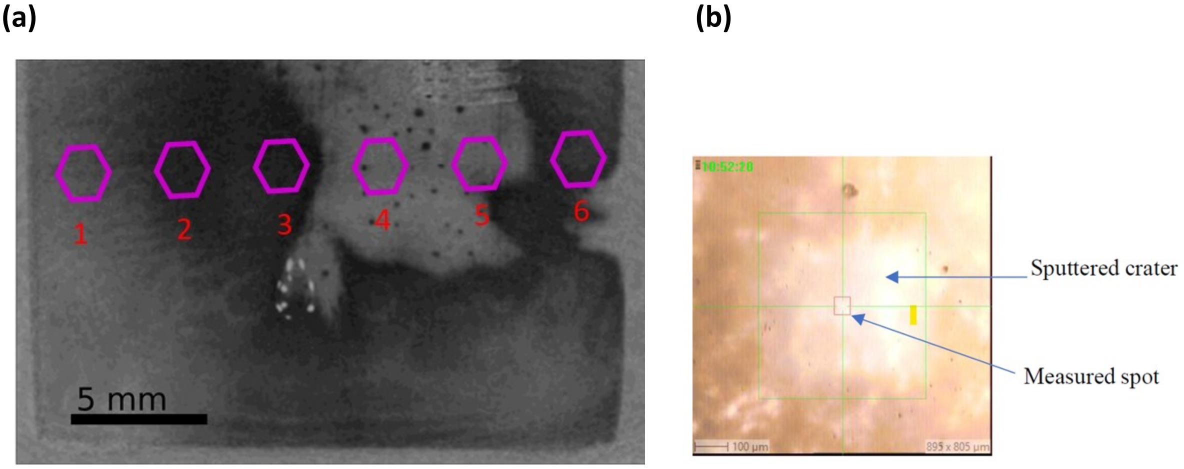

Figure S18: **Iron impurity distribution. (a)** Difference frame with respect to the discharged state of electrode SIL2 during charging. Spots (1) – (6) mark the locations of ToF-SIMS measurements (postmortem) across the electrode overlaid with the biphasic pattern formed during the beaker CV measurements presented in **Figure S4**. The artifact is attributed to the back reflection of the LED light source. **(b)** Optical image recorded after the ToF-SIMS analysis at one of the spots marked in panel (a), showing the sputtered crater and the measured area within the crater.

Figure S19 presents the SIMS spectrum from spot 4, integrated over the entire measurement at this spot. The main secondary ions are indium (In^+, $^{113}In^+$, and InH_2O^+) – from the ITO substrate; nickel (Ni^+) – from the $Ni(OH)_2$ layer; sodium (Na^+) and potassium (K^+) – from the aqueous electrolyte; and aluminum (Al^+) and iron (Fe^+) impurities. Other secondary ions are also observed (e.g., Al^+, Si^+, Ca^+, Mg^+ etc.), but their intensity is lower. **Table S4** presents the secondary ions and their respective intensities normalized by the total intensity of all the ions.

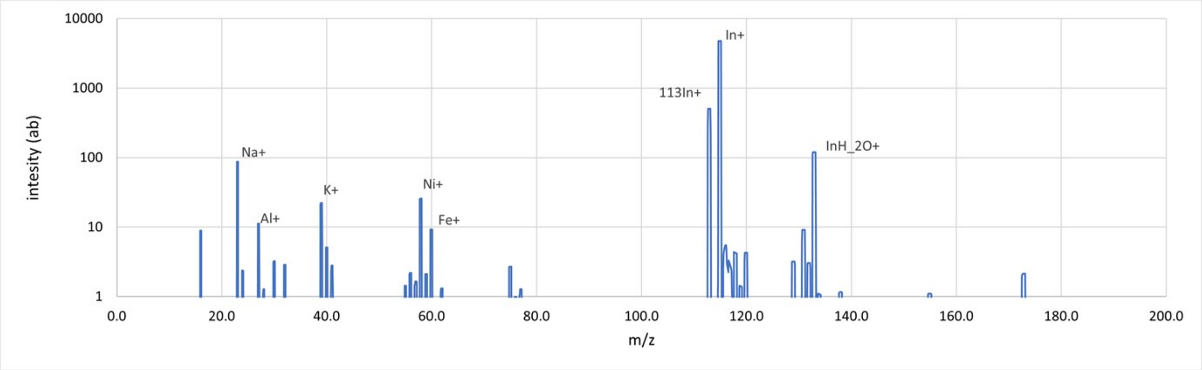

Figure S19: **SIMS spectrum**, integrated over the entire measurement, from spot (4).

Table S4: Secondary ions extracted from spot (4)

Center Mass (u)	Assignment	Area	Normalized intensity
	Total	31074491	1.0000
114.9	In^+	22494771	0.7239
112.9	$^{113}In^+$	2408605	0.0775
229.8	In^{2+}	1149238	0.0370
245.8	In_2O^+	643788	0.0207
23	Na^+	499234	0.0161
57.9	Ni^+	441289	0.0142
132.9	InH_2O^+	343426	0.0111
376.7	$In_3O_2^+$	248429	0.0080
39	K^+	245941	0.0079
250.8	$InSnO^+$	160255	0.0052
59.9	$^{60}Ni^+$	155742	0.0050
27	Al^+	96835	0.0031
40	Ca^+	50503	0.0016
28	Si^+	43453	0.0014
24	Mg^+	38488	0.0012
58.9	Co^+	33234	0.0011
45	$SiHO^+$	26334	0.0009
55.9	Fe^+	23512	0.0008
119.9	Sn^+	22876	0.0007
61.9	$^{62}Ni^+$	20103	0.0007
41	$^{41}K^+$	17260	0.0006
57	$CaOH^+$	14142	0.0005

Depth profiles of the key secondary ions of interest, In^+ (and In^{2+} whose intensity is closer to that of Ni^+) from the ITO substrate, Ni^+ from the $Ni(OH)_2$ layer, Fe^+ from iron impurities and K^+ from deposits from the KOH electrolyte are presented in **Figure S20(a)-(f)** for spots (1) – (6). The main ion is In^+ from the ITO layer. Its intensity increases from the $t = 0$ (surface), reaching a plateau after sputtering for ~20 s, which corresponds, approximately, to sputtering the entire $Ni(OH)_2$ layer.

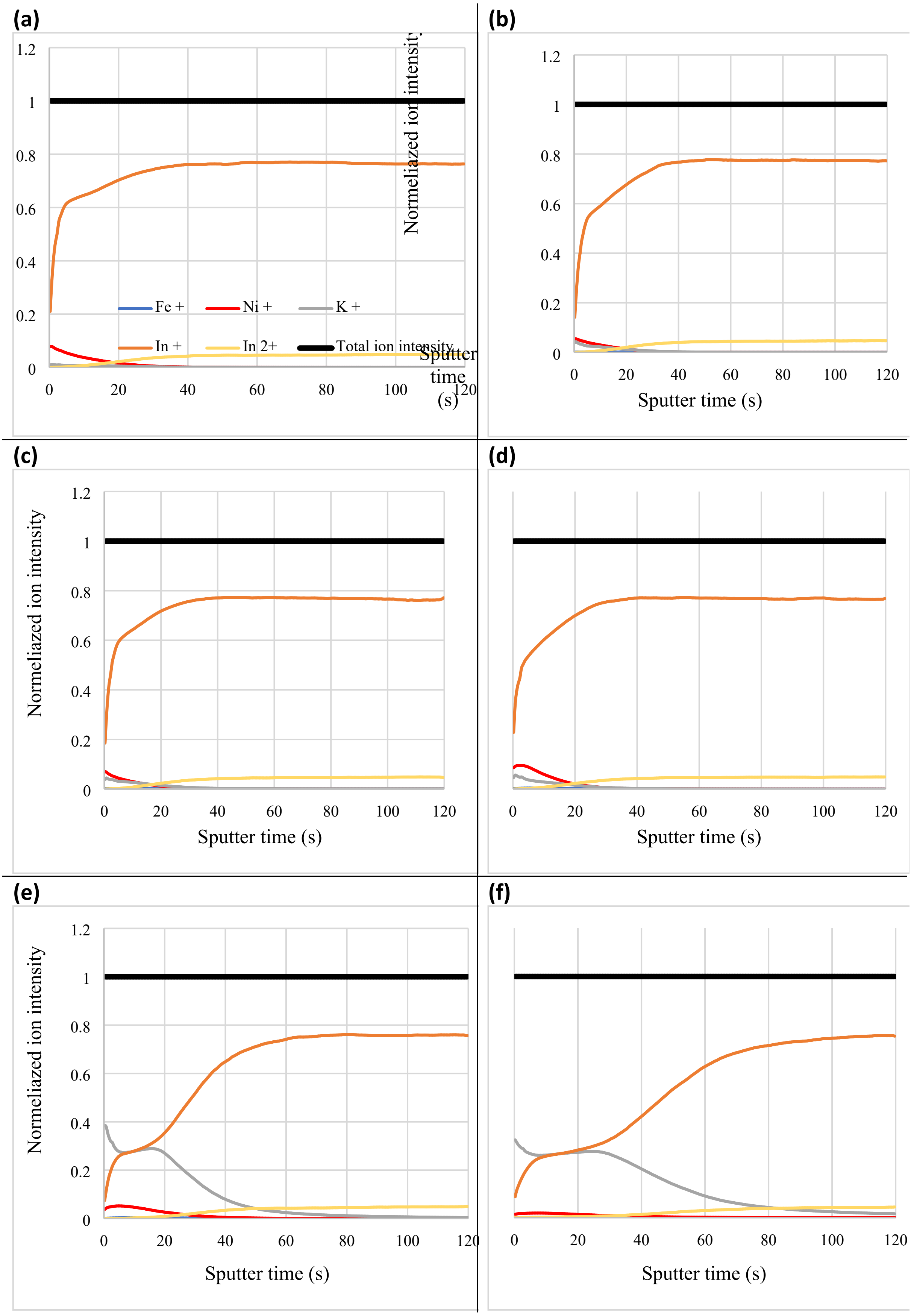

Figure S20: **Depth profiles** of key secondary ions of interest (as indicated by the legend) from **(a)** spot (1); **(b)** spot (2); **(c)** spot (3); **(d)** spot (4); **(e)** spot (5); **(f)** spot (6) in **Figure S18(a)**.

Looking at the $Ni(OH)_2$ layer, i.e., for sputter times between 0 and ~20 s, a similar trend is shown for spots (1) – (4) (**Figures S20(a) – (d)**), whereby the Ni^+ intensity (blue curves) > K^+ intensity (gray curves) > Fe^+ intensity (red curves). A markedly different trend is observed in spots (5) and (6) (**Figures S20(e)** and **(f)**), where K^+ intensity > Ni^+ intensity > Fe^+ intensity, suggesting excessive potassium deposits in these spots. Indeed, total intensity maps, integrated over the entire measurements (i.e., from t = 0 to 100 s), present excess K^+ and Mg^+ (and Si^+, not shown) in spots (5) and (6) compared to the other spots, as shown in **Figure S21**. This indicates that spots (5) and (6) do not accurately represent the $Ni(OH)_2$ layer but rather a mixture of the $Ni(OH)_2$ layer and excess deposits from the KOH electrolyte. Therefore, spots (5) and (6) are regarded as outliers that do not truly represent the impurity concentration within the $Ni(OH)_2$ layer.

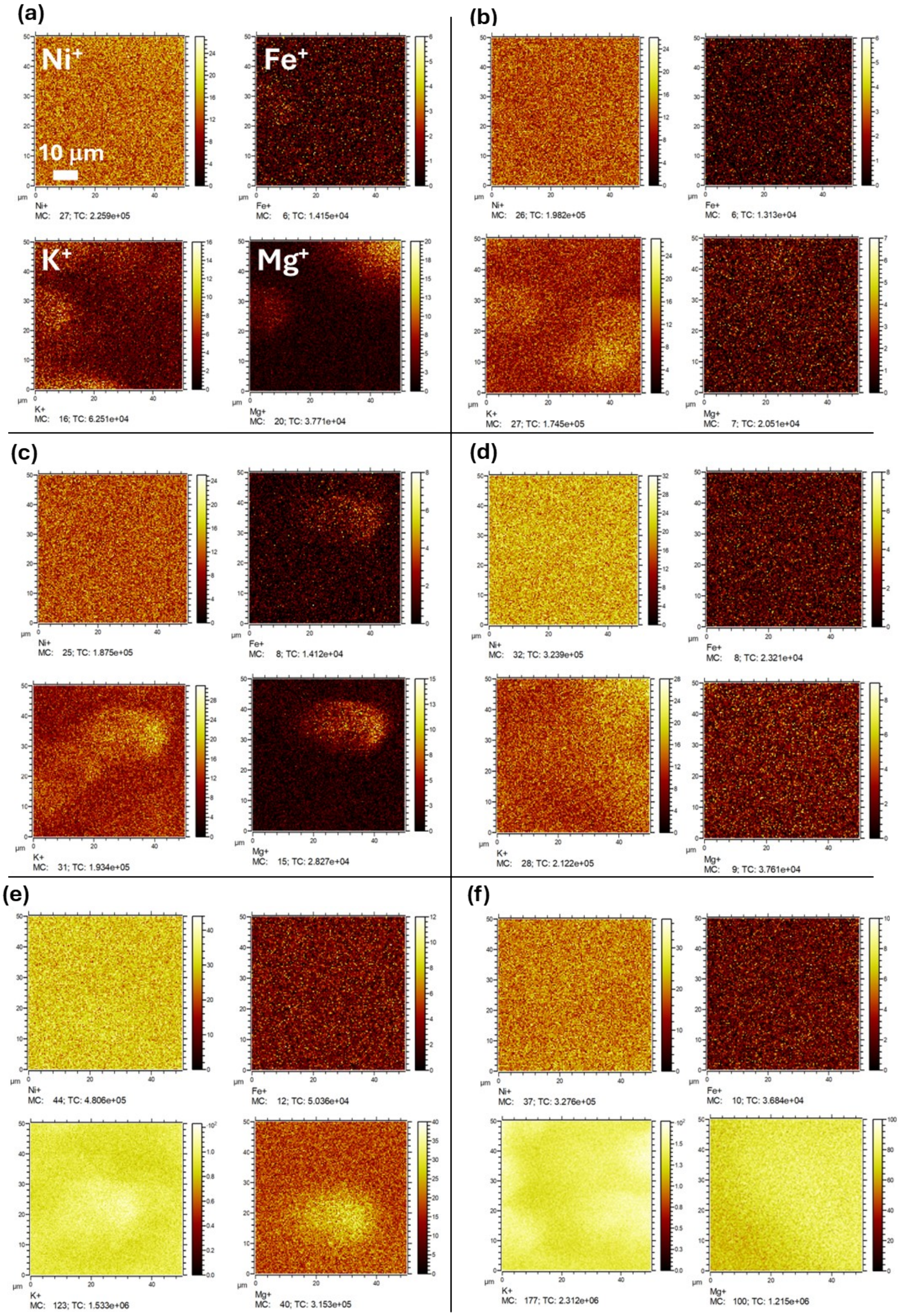

Figure S21: **Distribution maps** of key secondary ions of interest from **(a)** spot (1); **(b)** spot (2); **(c)** spot (3); **(d)** spot (4); **(e)** spot (5); **(f)** spot (6) in **Figure S18(a)**.

Considering the role of iron in enhancing oxygen evolution in NiOOH electrodes[3], we examine the Fe to Ni intensity ratio in spots (1) – (6), looking for a possible link between this ratio and the phase propagation pattern – shown in **Figure S18(a)**. To this end, we calculate the $Fe^+/(Ni^+ + Fe^+)$ intensity ratio, integrated over the $Ni(OH)_2$ layer thickness which corresponds to sputter times from $t = 0$ to 20 s (**Figure S20**). The results are summarized in **Table S5**, showing a uniform intensity ratio in spots (1) through (4). The intensity ratio is a bit higher in spots (5) and (6), but these spots are outliers as discussed before. Thus, the ToF-SIMS measurements show no evidence for a possible correlation between the phase propagation (**Figure S18(a)**) and iron impurity distribution (**Table S5**).

Table S5: $Fe^+/(Ni^+ + Fe^+)$ intensity ratio in spots (1) – (6)

	Peak area		$Fe^+/(Ni^+ + Fe^+)$ intensity ratio
	Fe^+	Ni^+	
Spot1	14238	267694	5.1%±0.3%
Spot2	13186	229187	5.4%±0.3%
Spot3	14192	217942	6.1%±0.4%
Spot4	23512	441289	5.1%±0.3%
Spot5	51501	674993	7.1%(outlier)
Spot6	37253	376910	9.0%(outlier)

* The error is estimated from the strand deviation between the intensity ratio of $NiOH^+$ to Ni^+ secondary ions, $NiOH^+/(Ni^+ + NiOH^+)$, in spots (1) – (4), integrated over $t = 0$ to 20 s. This estimation is justified by considering the largest source of error in the ToF-SIMS measurements which is the amount of impurity deposits from the electrolyte, that give rise to $NiOH^+$ secondary ions, in different measurement spots, as evidenced by the secondary ion distribution maps in **Figure S21**.

S6. Employing the optical data as a measure of charge for global and spatially-resolved charge analysis

For the quantitative analysis presented here, the $Ni(OH)_2$ layer should be thin enough to enable light transmission through the electrode such that the optical contrast between the fully charged (NiOOH) darkened state and the discharged ($Ni(OH)_2$) brightened state should be measurable by the dynamic range of the digital microscope, for imaging in transmission mode. Most of the electrodes examined in this study (**Table 1** in the article) were thin enough (~50 nm) to meet this requirement, and they were imaged in transmission mode, except for electrode ED1 that was imaged in reflection mode.

To quantitatively relate the optical data to actual charge (oxidized state) density distribution, we convert the video frames to 8-bit grayscale images and use the level of brightness of the pixels, $b(x,y,t)$ at location (x,y) and time t, to indicate the amount of charge, with darker being more charged. For imaging in transmission mode, $b(x,y,t)$ is proportional to the intensity of the light transmitted through the electrode with nickel (oxy)hydroxide layer thickness l_z. Defining $b_0(x,y)$ as the pixel brightness obtained by the incident light, without absorption in the sample, the Beer-Lambert decay of the light penetrating through the electrode is:

$$b(x,y,t) = b_0(x,y)e^{-\int_0^{l_z} \alpha(x,y,z,t)dz} \qquad \text{(eq S6.1)}$$

where $\alpha(x,y,z,t)$ is the optical absorption coefficient (weighted at the RGB wavelengths of the optical sensor within the digital microscope), which depends on the phase content (related to the Ni oxidation state) along the depth of the sample z. Luminescence and scattering effects are assumed to be negligible.

Providing that the change in $\alpha(x,y,z,t)$ during charging the electrode is proportional to the change in the local concentrations of Ni^{3+} and Ni^{2+}, where the former being a strong absorber and latter a weak absorber at visible (RGB) wavelengths[4], one could show that the local charge at point (x,y), integrated along the z dimension, is proportional to $ln\left(\frac{b(x,y,t_0)}{b(x,y,t)}\right)$ where t_0 designates the beginning of the charging measurement. This logarithmic relation between local brightness and local charge allows quantitative transformation of the optical data (i.e., pixel brightness) to local charge provided that the dynamic range of the camera is sensitive enough to monitor the local change in brightness through the entire thickness of the nickel (oxy)hydroxide layer. For this reason, the SILAR electrodes were made thin enough (~50 nm) to be translucent both before and after they were fully charged, see the charged regions of the SIL2 sample in **Figure S16(a)**.

For our thin film electrodes, linear approximation of the exponent in eq S6.1 is applicable. This simplifies the optical data processing and makes analyzed data more visually perceptive as only linear transformations are required in this case. Indeed, for SILAR samples SIL3 and

SIL4, linearization introduces small errors with an estimated upper limit of 4.6% and 8.8% respectively, in a fully charged state (where the linearization error is the highest). Therefore, it has insignificant impact on the analysis and derived conclusions. Assuming uniform electrode illumination, i.e., $b_0(x,y)$ being independent of the location (x,y), we use the local "darkening" level $\Delta\overline{b}(x,y,t)$ in the voxel $dx \cdot dy \cdot z$ at location (x,y) as the merit of local *z*-integrated charge.

$$\Delta\overline{b}(x,y,t) = b\left(x,y,t_0\right) - b(x,y,t) \qquad \text{(eq S6.2)}$$

To relate $\Delta\overline{b}(x,y,t)$ to the total charge, we must first define a value of "global darkness" $\langle\Delta\overline{b}\rangle(t)$ for each image of electrode surface at time *t*, as the average of $\Delta\overline{b}(x,y,t)$ over the electrode surface Ω imaged:

$$\langle\Delta\overline{b}\rangle(t) = \Omega^{-1}\iint_{\Omega} \Delta\overline{b}(x,y,t)dxdy \qquad (eq\,S6.3)$$

For practical computation, we replace the integrals in eq S6.3 by summations over the pixels in the exposed surface of the sample.

For a case study we use the galvanostatic charging measurement, shown in **Figure S22(a)**, and imaging, with selected video frames shown in **Figure S22(c)**, of electrode SIL4 presented in **Figure S5** and **Video 6**, which is a different sample than SIL3 that was analyzed in the article. $\langle\Delta\overline{b}\rangle(t)$ is plotted against the time-integrated current, $Q_{tot}(t) = \int I d\tau = It$ (since I is constant), in **Figure S22(b)**. Well before the OER onset, estimated from the fall-off of the potential vs. time charging curve of **Figure S22(a)**, the $\langle\Delta\overline{b}\rangle(t)$ vs. $Q_{tot}(t)$ curve (including the origin) shows an almost perfectly linear trend, at least before point 4, as seen by the dashed line in **Figure S22(b)**. This validates the implicit assumption used in this optical-imaging based work, especially detailed presentation of charge profiles at the propagating phase front (**Figure 4** in the article), that the charge (i.e., amount of oxidation) extracted from optical analysis (i.e., brightness changes, as defined by eq S6.2) of the video frames actually corresponds to the charge electrochemically spent on charging $Ni(OH)_2$ to NiOOH. It allows darkness-to-charge conversion factor *s* to be extracted from the average slope of $\langle\Delta\overline{b}\rangle(t)$ vs. $Q_{tot}(t)$ in the early linear region, assuming the entire surface exposed to electrolyte is within the field of view of the image:

$$\langle\Delta\overline{b}\rangle(t) = s \cdot Q_{tot}(t) \qquad \text{(eq S6.4)}$$

Informingly, point 4, while still appearing to be within the linearly increasing potential region of **Figure S22(a)**, nevertheless deviates from linearity in the $\langle\Delta\overline{b}\rangle(t)$ vs. $Q_{tot}(t)$ curve of **Figure S22(b)**. This suggests that oxygen evolution can begin even prior to the apparent saturation onset in the potential vs. time plot (**Figure S22(a)**). This could be expressed as Coulombic efficiency (CE), which is ideally unity in the linear region where there are negligible parasitic reactions and (nearly) all the current goes to charging $Ni(OH)_2$ to NiOOH. We extract it from the derivative of the $\langle \Delta \bar{b} \rangle (t)$vs. $Q_{tot}(t)$ curve, which is plotted as the second y-axis in **Figure S22(b)**. We remark as an aside, that such a continuous CE curve would be otherwise very time-consuming to extract by methods based on transient discharge for each point in the charging process[5], so the imaging technique could also offer potential as a new and quick way of evaluating CE for optically thin films.

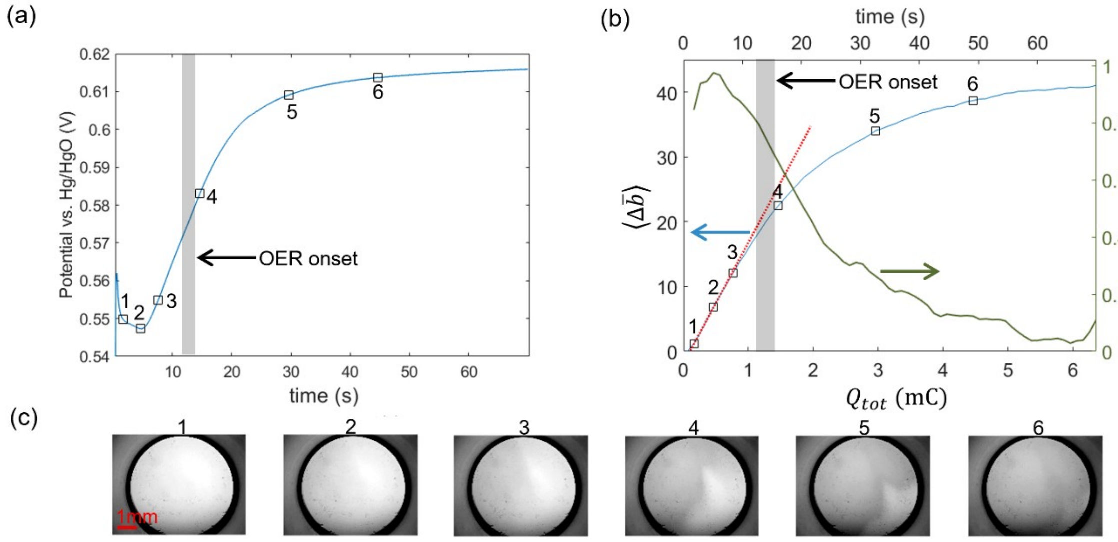

Figure S22. Darkness to charge conversion. (a) Potential vs. time for galvanostatic charging at a constant current of 100 μA of a $Ni(OH)_2$ electrode **SIL4** (50 SILAR deposition cycles, exposed area 0.28 cm^2), with selected points numbered. This is the same sample that is shown in **Figure S5** and **Video 6**. **(b)** Area-averaged darkness change $\langle \Delta \bar{b} \rangle (t)$, as defined in the text, with labelled points corresponding to the above panels. The horizontal scale was converted from time to passed charged, based on the sourced constant current of 100 μA. A linear fit to the near-linear region is shown with dashed red dots. The right axis shows the Coulombic efficiency computed from the ratio of the slope of $\langle \Delta \bar{b} \rangle (t)$ to passed charge $Q_{tot}(t)$, normalized to the maximum slope, which is assumed to be 1. **(c)** Gray scale video frames corresponding to the labelled points in panel (a). For the figure, display is enhanced for maximum contrast.

S7. Front propagation and uniform charging components

In the article we quantitatively characterize front propagation by plotting its position vs. time (**Figure 3**), and infer other front behaviors from qualitative inspection of a limited number of profiles. The key behaviors appeared to be that the front shape and width are maintained as the front propagates, and that a small (but observable) uniform charging component occurs in parallel with front propagation. Here, we show a fitting-based extension of the analysis that enables us to discern, quantitively, between the front propagation and uniform components that contribute to the overall charging. We quantitatively examine key spatiotemporal charging behaviors by systematic fitting of a relatively large number of sequential front profiles for the same galvanostatic scan as above. The diagonal cut which we selected along the observed front propagation direction, is shown in **Figure S23(a)**. The evolution of the local charge profile along the cut is depicted in **Figure S23(b)**. Qualitatively, it shows that a charged region forms between 0 and ~1.5 mm within the first 10 seconds of charging, which we call the front formation stage. Next, the charged region expands spatially, with the position of the front progressing in a linear manner, as indicated by the dashed line in **Figure S23(b).**

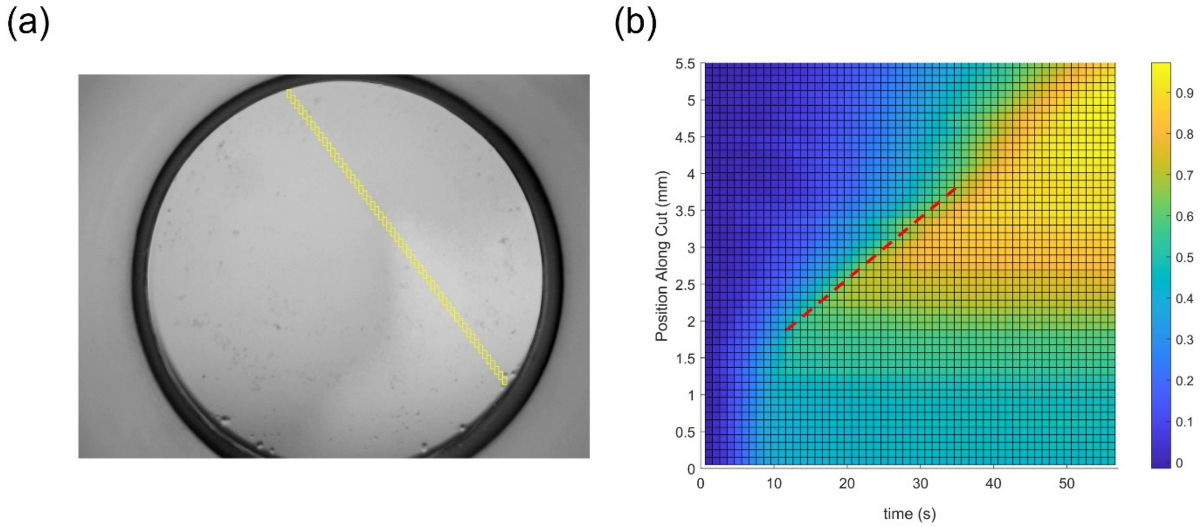

Figure S23. Cut for quantitative analysis. (a) Video frame of an intermediate time during charging of the SIL4 electrode (frame 5 in **Figure S22(c)**), showing a cut (yellow line) that the charge profiles were obtained for. **(b)** 2D heat map representation of the charge evolution along the cut, with the brighter region indicating more charged, as indicated by the color bar to the right. The color values are scaled by the maximum local darkness throughout the charging measurement. The dashed line is a guide to the eye to highlight the constant front propagation velocity

To analyze quantitatively the front and its dynamics of propagation along the cut, we normalize the data for all times by the maximum charge profile during charging (vertical cut in **Figure S23(b)** at t = 55s). This normalizes out possible sample lateral heterogeneities. Then we use a relatively simple and convenient form of the hyperbolic tangent function to describe the charge profile:

$$y = A \cdot \tanh\left(\frac{x - x_0}{w/\sqrt{2}}\right) + z_{offset} \tag{eq S7.1}$$

The parameters in eq S7.1 quantitatively define the main attributes of the charge front (all normalized to maximum local capacity), namely the height of the charge difference between charged and uncharged regions (2A), the characteristic width of the transition region (w), the front position along the cut (x_0), and a uniform charge offset (z_{offset} - A), which was observed to exist and grow in the profiles presented in the article. For alternative visualization, the respective variables of front height and uniform-charged height can be recast as the total height (from zero) in the charged region (A+z_{offset}), and fraction of this total which is uniform charge ($\{z_{offset} – A\} / \{z_{offset} + A\}$).

The profiles for all 64 frames sampled over the charging scan, along with the fits to eq S7.1, are shown in **Figure S24.** Within the scatter of points, the hyperbolic tangent is an excellent fit to the edge step of the normalized profiles up to t~ 32 s. After that, the edge is less well defined since it runs into the border of the diagonal cut, so the fit parameters are more ambiguous. This is reflected in the error bars of the fit parameters (expressed as fundamental front attributes, as described above) in **Figures S25(a)-(d)**. Save for position, the error bars dramatically increase for times beyond the mid-30 s.

Quick inspection of **Figure S25** shows consistency with the qualitative and quantitative observations made in the article (**Figure 3**), namely that the front propagates with near-constant velocity (**Figure S25(a)**) and maintains its shape, i.e., width and height (**Figures S25(b)**,**(c)**, respectively), during such propagation, and that there is an growing uniform charging component (**Figure S25(d)**). Beginning in the front propagation stage (at t = 8 s, **Figure S25(a)**), the uniform charging component continually increases to significant values (**Figure S25(d)**).

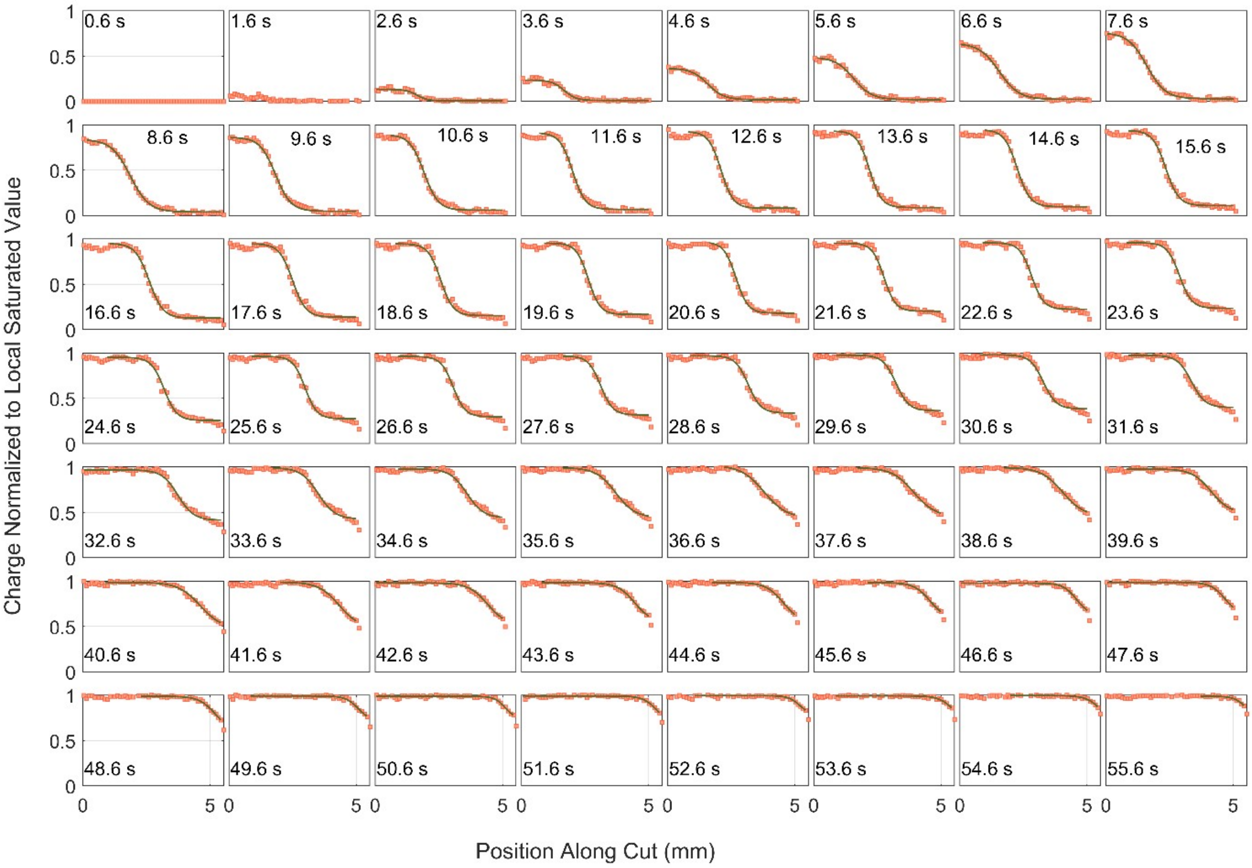

Figure S24. Fitting charge profiles. Normalized charge profiles along the diagonal cut (in **Figure 23(a)**) and fit of the edge (solid green line) for the time points evaluated during galvanostatic charging.

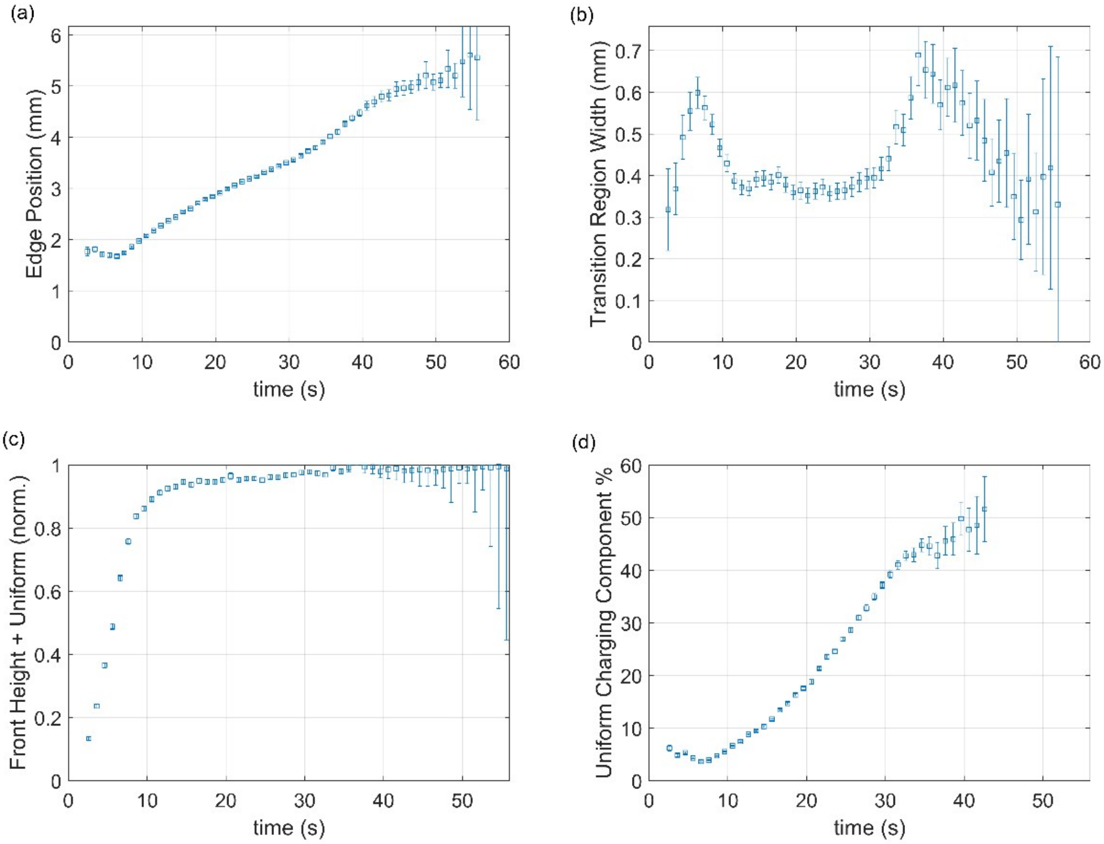

Figure S25. Fitted front profile parameters of the front descriptors extracted from eq S6.1 as described in the text. **(a)** edge position, **(b)** transition region width, **(c)** combined charge profile height of charged region, **(d)** fraction of the latter which is from the uniform charging component, plotted as a percentage.

S8. Surface photovoltage (SPV) measurements

A Kelvin probe was used to measure the surface photovoltage (SPV) of a $Ni(OH)_2$ sample in the reduced (after aging) and oxidized states by measuring the contact potential difference (CPD) between the electrode and the Ti probe (5 mm diameter) upon shining the elecrode with above bandgap illumination using a hand held violet laser pointer (λ = 405±10 nm, P $\approx$ 5 mW). To detremine the conductivity type by SPV, the $Ni(OH)_2$ layer should be sufficiently thick to remove any possible SPV effect from the substrate[6]. Electrodeposition on a metallic Ni foil substrate, using 0.1 mol/L nickel nitrate solution, resulted in thick layer of nickel hydroxide estimated to be 1 µm thick. The electrode was aged by leaving it in 1 M KOH electrolyte for two days (at open circuit). It was then cleaned and thoroughly air dried before placing it in the Kelvin probe apparatus (**Figure S26(a)**), showing a whitish color which obscured the underlying substrate.

The CPD change was measured during shining the aged electrode with the violet laser, yielding the SPV = CPD(light) − CPD(dark) in steady state. After this measurement, the electrode was electrochemically oxidized (**Figure S26(b)**), showing the standard oxidation curve at expected potential, thus confirming the β-NiOH)$_2$ phase before oxidation, and resulting in a black β-NiOOH layer after oxidation (**Figure S26(c)**). The same SPV measurement procedure used for the unoxidized sample was repeated on the oxidized sample.

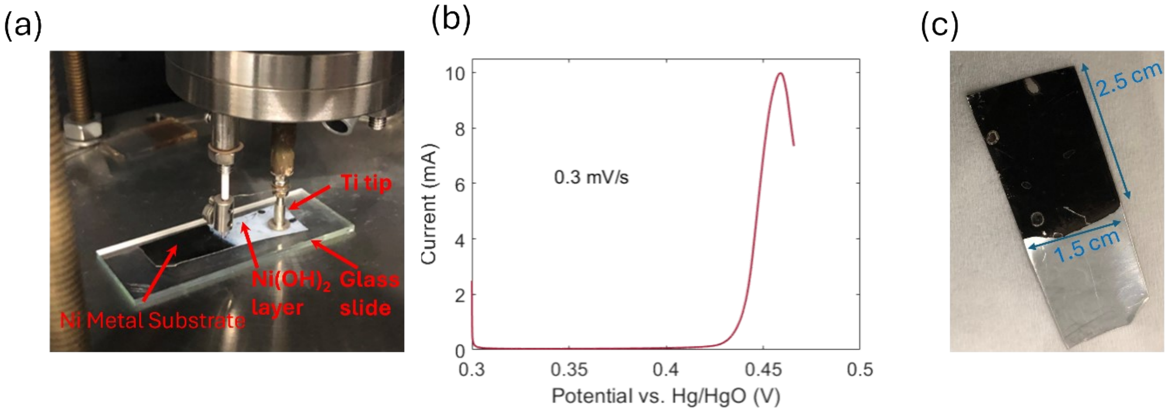

Figure S26. Surface photovoltage (SPV) measurement setup. (a) Setup of $Ni(OH)_2$ electrode under the Kelvin probe tip. **(b)** Charging curve when oxidizing the electrode. The potential was ramped up by 3 mV/s. **(c)** Photograph of the oxidized electrode.

The SPV response of the unoxidized and oxidized electrodes is shown in **Figure S27**. The unoxidized electrode showed a substantial increase in CPD of ~ 100 mV which stopped increasing as soon as the light was turned off. The positive sign of the CPD change suggests downwards band-bending at the surface consistent with a *p*-type semiconductor[6]. We interpret the long relaxation time (10 hours, not shown) to suggest long-lived surface states. In contrast, the oxidized sample showed a much weaker SPV (nearly negligible), and the CPD reverted back immediately (< 1 min) after the light was turned off, suggesting a qualitatively different character that is more akin with a degenerately-doped semiconductor, i.e., a semi-metallic electrode. For example, in another study[7] we observed strong SPV response for undoped and Zn-doped hematite electrodes, while highly Ti-doped hematite showed a weak SPV.

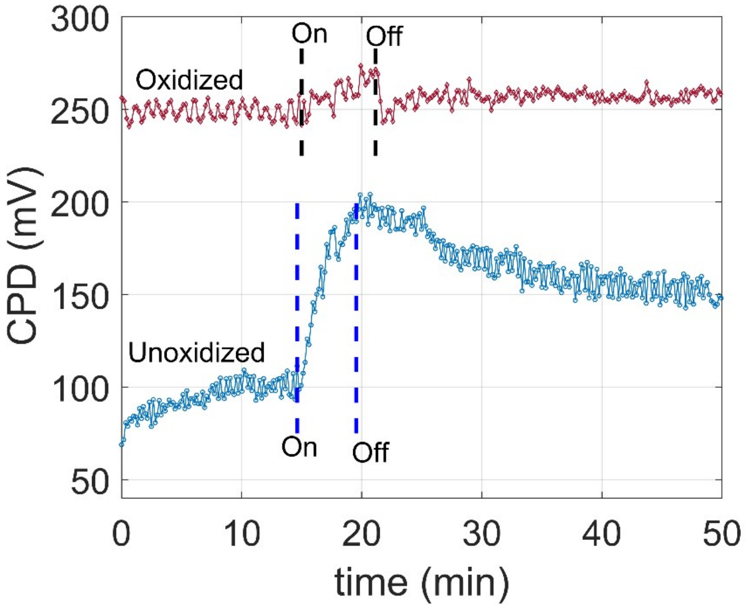

Figure S27. **SPV response of unoxidized and oxidized electrodes.** Comparison of CPD difference upon illumination between unoxidized $Ni(OH)_2$ and the same sample oxidized to mostly NiOOH. The time the laser pointer was turned on and off is shown as the dashed vertical lines. The upper curve was time-shifted so as to roughly align the on-off times for ease of comparison.

S9. Model derivation

The model encompasses two phases prescribed by a Chan-Hilliard-type order parameter and mobile charge carriers which are protons and electrons, in analogy to organic photovoltaic modeling.[8] The order parameter obeys a double well potential of a fully discharged (reduced) $Ni(OH)_2$ electrode and a fully charged (oxidized) NiOOH electrode. The free energy involving H^+ concentration (p), e^- concentration (n), electrostatic potential φ, and the volume fractions of Ni^{2+} ($Ni(OH)_2$) and Ni^{3+} (NiOOH) (χ_a and χ_b), respectively, reads as follows:

$$\mathcal{E} = \mathcal{E}_{mixing} + \mathcal{E}_{entropy} + \mathcal{E}_{electrostatic} + \mathcal{E}_{charge\ affinity}, \qquad \text{(eq S9.1)}$$

where

$$\mathcal{E}_{mixing} = \int_\Omega f_{mixing} d\Omega = c\int_\Omega \left[\beta W(\chi_b - \chi_a) + E_0\kappa^2|\nabla(\chi_b - \chi_a)|^2\right]dr, \qquad \text{(eq S9.2a)}$$

$$\mathcal{E}_{entropy} = \int_\Omega f_{entropy} d\Omega = kT\int_\Omega \left[c\chi_a ln x_a + c\chi_b ln x_b + n ln\frac{n}{c} + p ln\frac{p}{c}\right]dr, \qquad \text{(eq S9.2b)}$$

$$\mathcal{E}_{electrostatic} = \int_\Omega f_{electrostatic} d\Omega = \int_\Omega \left[q(p - n)\varphi + \frac{\epsilon|\nabla\varphi|^2}{2}\right]dr, \qquad \text{(eq S9.2c)}$$

$$\mathcal{E}_{charge\ affinity} = \int_\Omega f_{charge\ affinity} d\Omega = 2\zeta\int_\Omega \left[p{\chi_b}^2 + n{\chi_a}^2\right]dr, \qquad \text{(eq S9.2d)}$$

and $W(\chi_b - \chi_a) = \left(1 - (\chi_b - \chi_a)^2\right)^2$ is the double-well potential with minima corresponding to the $Ni(OH)_2$/NiOOH states; the meaning and dimensons of parameter value are summarized in **Table S6**.

Next, we write the respective chemical potentials:

$$\mu_{Ni^{2+}} = \frac{\delta\mathcal{E}}{\delta(c\chi_a)} = \frac{1}{c}\left[ckT + ckTln(\chi_a) + 4\zeta n\chi_a - \left(c\beta W' - 2cE_0\kappa^2\nabla^2(\chi_b - \chi_a)\right)\right], \qquad \text{(eq S9.3a)}$$

$$\mu_{Ni^{3+}} = \frac{\delta\mathcal{E}}{\delta(c\chi_b)} = \frac{1}{c}\left[ckT + ckTln(\chi_b) + 4\zeta p\chi_b + \left(c\beta W' - 2cE_0\kappa^2\nabla^2(\chi_b - \chi_a)\right)\right], \qquad \text{(eq S9.3b)}$$

$$\mu_{H^+} = \frac{\delta\mathcal{E}}{\delta p} = kT + kTln\left(\frac{p}{c}\right) + q\varphi + 2\zeta\chi_b^2, \qquad \text{(eq S9.3c)}$$

$$\mu_{e^-} = \frac{\delta\mathcal{E}}{\delta n} = kT + kTln\left(\frac{n}{c}\right) - q\varphi + 2\zeta\chi_a^2, \qquad \text{(eq S9.3d)}$$

and the potential which results in the Poisson's equation

$$\frac{\delta\mathcal{E}}{\delta\varphi} = 0 = q(p - n) - \epsilon\nabla^2\varphi \qquad \text{(eq S9.4)}$$

Using the order parameter definition $u = \chi_b - \chi_a$, where $\chi_a \equiv \frac{1 - u}{2}$ and $\chi_b \equiv \frac{1 + u}{2}$, we obtain the fluxes from the Onzager's relations (for details, see[5]):

$$J_n = -\frac{D_n}{kT} n \nabla \mu_{e^-} = -D_n \left[\nabla n - \frac{q}{kT} n \nabla \varphi - \frac{\zeta}{kT} n (1-u) \nabla u \right], \qquad \text{(eq S9.5a)}$$

$$J_p = -\frac{D_p}{kT} p \nabla \mu_{H^+} = -D_p \left[\nabla p + \frac{q}{kT} p \nabla \varphi + \frac{\zeta}{kT} p (1+u) \nabla u \right], \qquad \text{(eq S9.5b)}$$

$$J_u = -2 \frac{D_u}{kT} c \chi_a \chi_b \left[\nabla \mu_{Ni^{3+}} - \nabla \mu_{Ni^{2+}} \right] = -D_u c \left[\begin{aligned} & \nabla u + \frac{\zeta}{ckT} (1-u^2) (\nabla p (1+u) - \nabla n (1-u) + (p - \\ & \qquad (1-u^2) \left(\frac{\beta}{kT} W'' \nabla u - \frac{E_0 \kappa^2}{kT} \nabla^3 u \right) \end{aligned} \right. \qquad \text{(eq S9.5c)}$$

.

Finally, we introduce the dissipative reaction term that follows the law of mass action for the redox reaction $NiOOH + H^+ + e^- \rightleftarrows Ni(OH)_2$ at the phase front:

$$R = c k_f (1-u^2) \left(np \frac{1+u}{2} - \frac{1}{K} \frac{1-u}{2} \right), \qquad \text{(eq S9.6)}$$

where k_f is the forward reaction rate constant and K is the equilibrium constant. Here, the $1-u^2$ term localizes the reaction to the interface between the phases.

By introducing dimensionless quantities,

$$\tilde{t} = \frac{t}{\tau}, \quad \tilde{r} = \frac{r}{l}, \quad \tilde{n} = \frac{n}{c}, \quad \tilde{p} = \frac{p}{c},$$
$$\tilde{\beta} = \frac{\beta}{kT}, \quad \lambda = \frac{kTl^2}{E_0 \kappa^2}, \quad \tilde{\zeta} = \frac{\zeta}{kT}, \quad \tilde{\varphi} = \frac{q\varphi}{kT},$$
$$\tilde{\epsilon} = \frac{q^2 \epsilon}{kTcl^2}, \quad \tilde{k}_f = \tau c^2 k_f, \quad \tilde{K} = \frac{K}{c^2}, \quad \tilde{D}_{u,n,p} = \frac{\tau D_{u,n,p}}{l^2},$$

we obtain the dimensionless model equations (**eq 1** in the main text).

The model is solved numerically via Comsol Multiphysics 5.2 as a system of elliptic-parabolic partial differntial equations with a dummy variable, $\psi = \nabla^2 u$. Specifically we use the MUMPS direct solver and adaptive BDF (2^{nd}-5^{th} order) for time integration. In 1D, we employ an equidistant mesh with an element size 0.005, while in 2D, we use an automatically generated triangular grid with a maximum element size 0.1, minimum element size 0.012, curvature factor 0.2, and resolution of narrow regions 1. Tolerance is set up to 10^{-6}. Parameter values are prescribed in **Table S7.**

Table S6. Quantities in the model and their fundamental dimensions, expressed by length L, time T, energy E, and charge C.

Quantity	Description	Dimensions
r	Spatial variable	L
t	Time	T
c	Ni atom density	L^{-3}
n	Mobile electron density	L^{-3}
p	Mobile proton density	L^{-3}
φ	Electric potential	$C^{-1}E$
u	Phase order parameter	I
kT	Energy scaling factor	E
β	Phase interaction coefficient	E
ζ	Phase-Charge affinity coefficient	E
$E_0\kappa^2$	Interfacial energy density	$L^{-2}E$
q	Elementary charge	C
ϵ	Permittivity	$L^{-1}E^{-1}C^2$
k_f	Forward reaction rate constant	$L^6\mathrm{T}^{-1}$
K	Equilibrium constant	L^{-6}
D_u	Phase diffusion coefficient	$L^2\mathrm{T}^{-1}$
D_n	Mobile electron diffusion coefficient	$L^2\mathrm{T}^{-1}$
D_p	Mobile proton diffusion coefficient	$L^2\mathrm{T}^{-1}$

Table S7. Values of the scaled model parameters used in simulations

Dimensionless model parameter	Value
D_u	10^{-2}
D_n	10
D_p	1
β	50
λ	15
ζ	30
k_f	10^2
K	10^5
ϵ	0.05

Complementary to the proton and electron profile presneted in **Figure 4** in the article, **Figure S28** presents proton and electron profiles from simulations at times t_1 and t_2 and currents I = 10^{-3} and 10^{-2} in **Figure 5**:

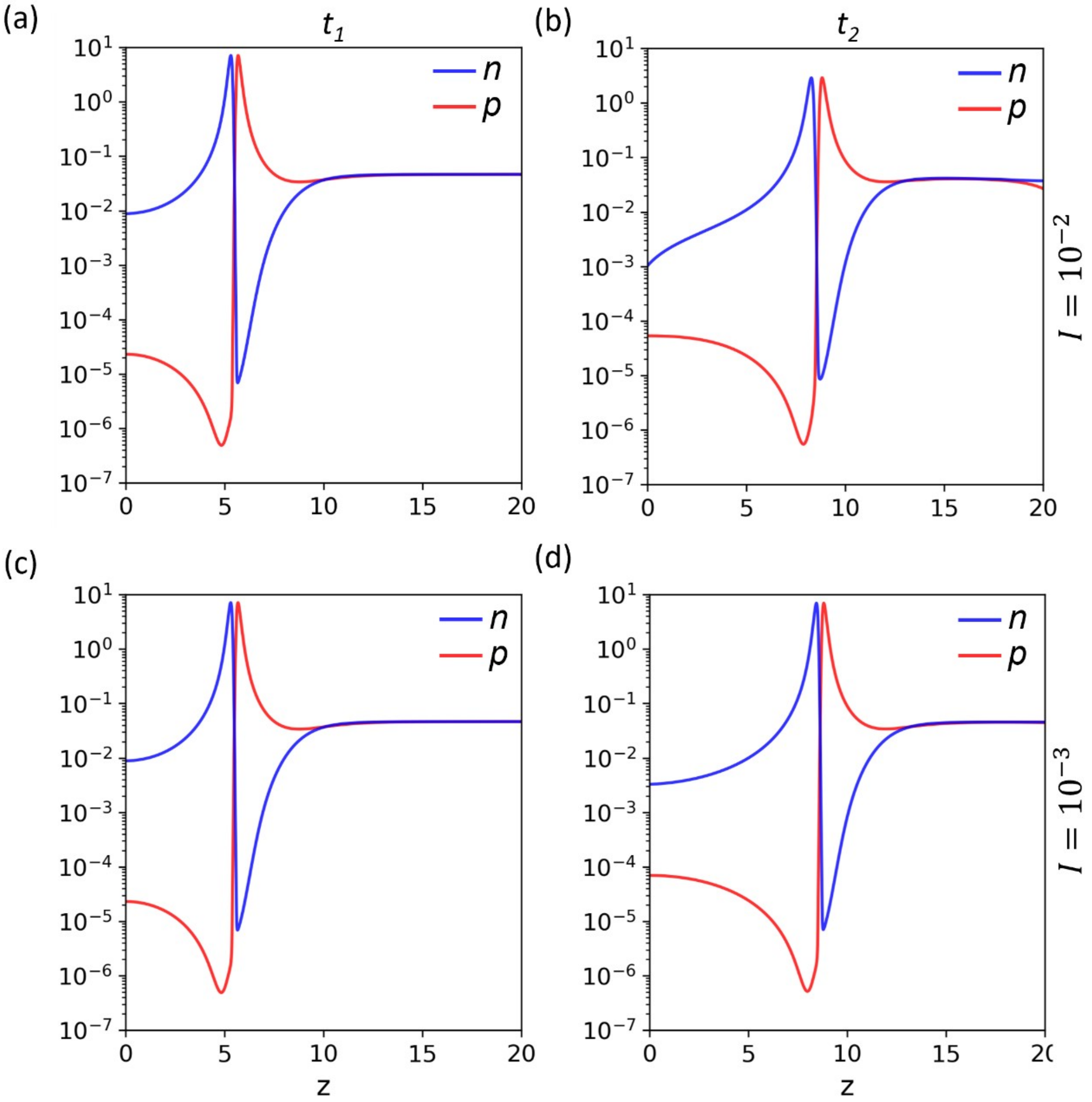

Figure S28. Proton (p) and electron (n) charge density profiles obtained in 1D charging simulations. Charge density profiles (in a semilogarithmic scale) at times t_1 **(a)**,**(c)** and t_2 **(b)**,**(d)** for $I = 10^{-2}$ **(a)**,**(b)** and $I = 10^{-3}$**(c)**,**(d)**.

References:

1. G. J. C. Carpenter and Z. S. Wronski, *Micros. Today*, 2021, **29**, 26–29.

2. C. F. Holder and R. E. Schaak, *ACS Nano*, 2019, **13**, 7359–7365.

3. L. Trotochaud, S. L. Young, J. K. Ranney and S. W. Boettcher, *J. Am. Chem. Soc.*, 2014, 136, 6744-6753.

4. Y. Abe, T. Suzuki, M. Kawamura, K. Sasaki and H. Itoh, *Solar Energy Mater. Solar Cells*, 2012, **99**, 38–42.

5. H. Dotan, A. Landman, S. W. Sheehan, K. D. Malviya, G. E. Shter, D. A. Grave, Z. Arzi, N. Yehudai, M. Halabi, N. Gal, *et al.*, *Nat. Energy*, 2019, **4**, 786–795.

6. L. Kronik and Y. Shapira, *Surf. Sci. Rep.*, 1999, **37**, 1-206.

7. A. Kay, D. A. Grave, D. S. Ellis, H. Dotan and A. Rothschild, *ACS Energy Lett.*, 2016, **1**, 827–833.

8. A. Z. Shapira, N. Gavish and A. Yochelis, *EPL*, 2019, **125**, 38001.